UNCLASSIFIED

AD NUMBER
ADB002056
LIMITATION CHANGES
TO: **Approved for public release; distribution is unlimited.**
FROM: **Distribution authorized to U.S. Gov't. agencies only; Test and Evaluation; 25 FEB 1975. Other requests shall be referred to Naval Sea Systems Command, code 06412, Washington, DC 20360.**
AUTHORITY
usnssc ltr, 2 jul 1976

THIS PAGE IS UNCLASSIFIED

Report HA 113-74

Hydroacoustics Project 2018
Navy Project SF111 121 1302

FINAL REPORT

FLEXURAL MODE AND HYDROACOUSTIC TRANSDUCER STUDY

Contract N00024-73-C-1170

STATEMENT B
DISTRIBUTION LIMITED TO U. S. GOVERNMENT T&E 25 FEB 1975
AGENCIES ONLY; OTHER REQUESTS FOR THIS DOCUMENT
MUST BE REFERRED TO NAVSEA 06H12
Wash., D.C. 20360

August 1974

DDC
RECEIVED
MAR 3 1975
B

HYDROACOUSTICS INC.

Report HA 113-74

Hydroacoustics Project 2018
Navy Project SF111 121 1302

FINAL REPORT

FLEXURAL MODE AND HYDROACOUSTIC TRANSDUCER STUDY

Contract N00024-73-C-1170

August 1974

Report HA 113-74

Hydroacoustics Project 2018-4
Navy Project SF111 121 1302

FINAL REPORT

FLEXURAL MODE AND HYDROACOUSTIC TRANSDUCER STUDY

E. M. Cliffel
R. F. DeLaCroix
P. J. Singh

August 1974

Contract N00024-73-C-1170

R. L. Selsam
Director of Engineering

J. V. Bouyoucos
President

Submitted to
Department of the Navy
Naval Ships System Command
Washington, D.C. 20360
Attention: Code PMS 302-42

HYDROACOUSTICS INC.

321 NORTHLAND AVE. P.O. BOX 3818 ROCHESTER, N.Y. 14610

(716) 544-2350

TABLE OF CONTENTS

TABLE OF CONTENTS

CONTINUED

Page

LIST OF ILLUSTRATIONS

LIST OF ILLUSTRATIONS (Continued)

LIST OF ILLUSTRATIONS (Continued)

TABLES

ADMINISTRATIVE INFORMATION

This project is being sponsored by NAVSHIPS CODE PMS 302-42 under contract N00024-73-C-1170. The Project Serial Number is SF111 121 302. The NAVSHIPS project engineer is Robert Kolesar. Additional technical guidance has been provided by Dr. C. H. Sherman, Dr. R. S. Woollett and C. L. LeBlanc of NUSC-NLL.

1.0 SUMMARY

This project is a continuation of a development program for flexural mode transducers and hydroacoustic technology at Hydroacoustics Inc. Mathematical models for general flexural mode transducers and hydroacoustic power oscillators developed in the preceding projects have been used to generate design trade-off data for bender hydrophones and a class of sound sources which operate on the ambient sea pressure head.

The hydrophone trade-off analysis shows that bilaminar hydrophones are generally preferred over the trilaminar configuration, the edge support for the bender can be designed such that it has little effect on the hydrophone performance when operating air backed but has a significant effect on liquid-filled, pressure compensated hydrophone performance, and thicker discs are preferred over thinner discs in the design of liquid filled, pressure compensated hydrophones. Detailed design curves are presented which quantify the trade-off between sensitivity, impedance, bandwidth, and operating depth for many combinations of hydrophone geometry.

The results from the design trade-off study of hydroacoustic power oscillators describe quantitativley how the input and output power and harmonic content change when the design parameters valve stroke, supply pressure, porting length, load resistance, and filter characteristics are varied. This trade-off data enables the designer to select the proper combination of design parameters to give the desired performance of the hydroacoustic power oscillator.

2.0 BENDER HYDROPHONE DESIGN TRADEOFF STUDY

Piezoelectric elements excited in their flexural mode have been used as hydrophones for the last 20 or 30 years, and because of their good coupling to the medium, interest in them remains high. Flexural mode (or bender) hydrophones using piezoelectric discs bonded together or to a metalic supporting structure can have a low characteristic acoustic impedance and low resonant frequency giving good power transfer to their preamplifier making them excellent low frequency hydrophones. With proper pressure compensation this type of hydrophone can be used at great depth with no particular sacrifice in sensitivity. This section of the report presents basic design and tradeoff data for bender hydrophones and shows how these relationships are affected by various edge supports and pressure compensation. Table 2.1 is a glossary of symbols and nomenclature used in this tradeoff study.

Figure 2.1 shows the basic geometries considered in this report. The upper portion of this figure shows the symmetrical trilaminar hydrophone where the total ceramic thickness t_c is split equally on either side of the backing material with a thickness t_b. If no backing material is used, this geometry reduces to the simple symmetrical bilaminar or bimorph hydrophone. The asymmetrical bilaminar hydrophone shown in the lower portion of this figure has all of the ceramic material on one side of the backing. When this geometry is used with the water on the ceramic side, the hydrostatic pressure will provide a compressive bias stress in the ceramic. As shown later in this section, this lets the asymmetrical bilaminar hydrophone be used to greater depths than the trilaminar hydrophone.

TABLE 2.1

SYMBOLS USED IN SECTION 2.0

a - disk radius

A - disk area (πa^2)

h - disk total thickness

t_b - metal backing thickness

t_c - total ceramic thickness

t_n - reference plane coordinate

ρc - density of ceramic

ρb - density of metal backing

E^b - modulus of elasticity for the metal backing

E^c - $1/S^E_{11}$ ceramic material

S^D_{11} - elastic compliance coefficient at constant charge density

S^D_{12} - elastic compliance coefficient at constant charge density

S^D_{44} - elastic compliance coefficient at constant charge density

g_{31} - piezoelectric constant

ε^T_{33} - dielectric constant at constant stress (free)

k_p - planar coupling coefficient

σ^D - (S^D_{12}/S^D_{11}) Poison's ratio of ceramic at constant charge density

TABLE 2.1 (Continued)

σ^E - (S_{12}^E/S_{11}^E) Poison's ratio of ceramic at constant voltage (short circuit)

σ^b - Poison's ratio of metal backing

M - $(M_e)_h$ - hydrophone receiving sensitivity

C_{LOW} - low frequency capacitance

f^R - short circuited, unloaded resonant frequency

D - Maximum depth based on maximum radial stress in the ceramic material

t_h - hinge thickness

r_h - hinge outside radius

C_{DH} - acoustical compliance of the disc and hinge air backed and open circuited

C_T - acoustical compliance of pressure compensation cavity

T_h - maximum radial tensile stress in the hinge

T - maximum radial stress in the ceramic of the bender (compressive stress for bilaminar geometry or tensile stress for trilaminar geometry)

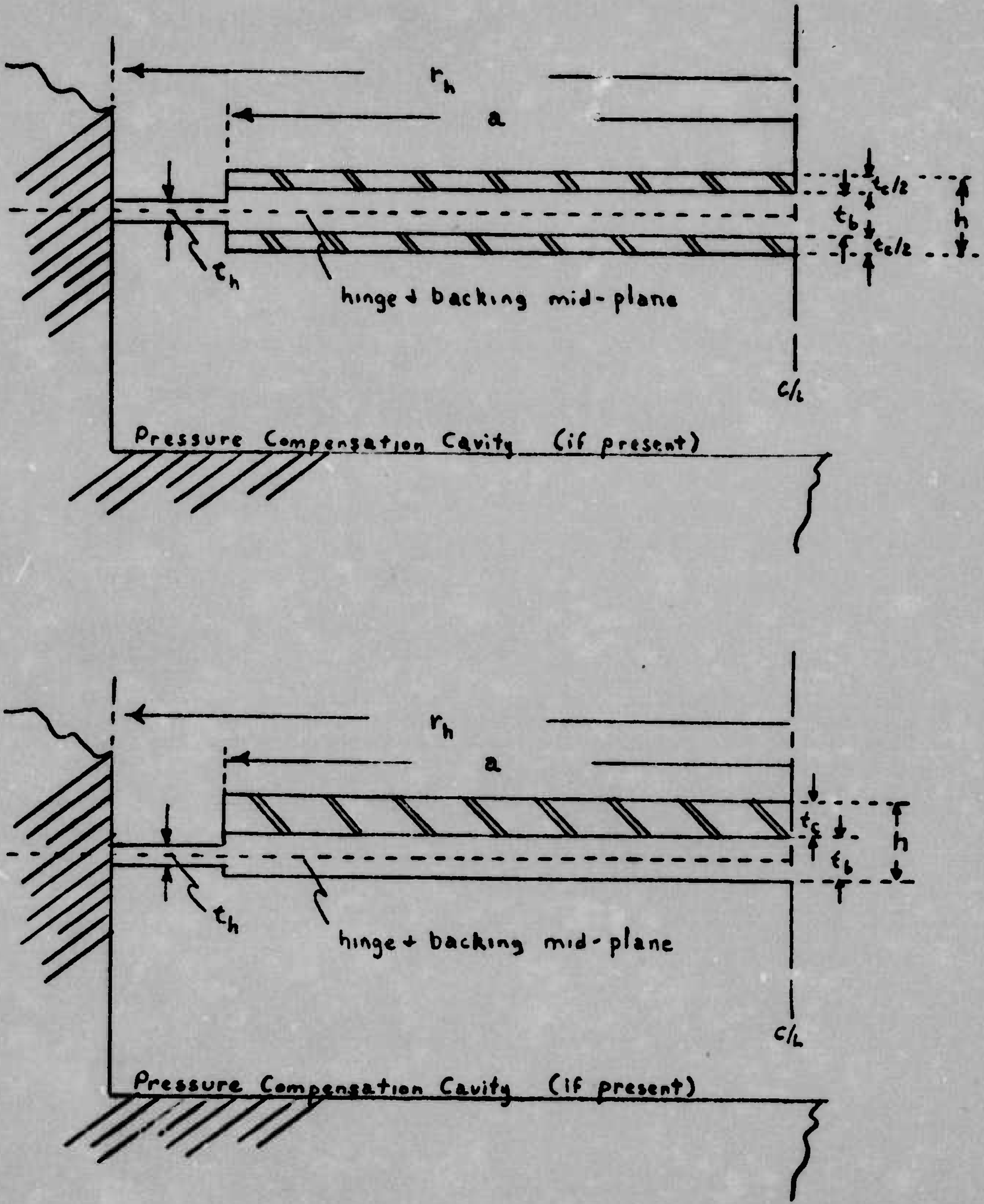

Figure 2.1 Basic Geometry for Trilaminar and Bilaminar Bender Hydrophone Designs Considered in this Report.

Since the dipole sensitivity of a single flexing disc is low, the single-ended hydrophones considered here are enclosed in a massive housing which acoustically terminates one side in a closed cavity with stiff walls. This cavity can be at atmospheric pressure or can be coupled through a high acoustic impedance to the ambient pressure providing pressure compensation. Two flexing discs can be used in one hydrophone to provide increased sensitivity or to measure velocity rather than pressure. Many of the results described here can be applied to both single and double-ended hydrophones.

Some of the hydrophones discussed in this report use the simple hinge edge support shown in Figure 2.1, and other data assumes a simply supported edge. In the latter case the bender is assumed to be simply supported at radius a and no hinge is used. When air backed benders are discussed, the pressure compensation cavity shown here is assumed to have zero stiffness, and the average pressure in the cavity is assumed to be zero.

2.1 DESCRIPTION OF THE PROBLEM

Six nondimensional design parameters are defined from Figure 2.1 to describe the geometry of the bender hydrophone. Three are used to describe the disc: the ratio of total disc thickness to disc radius (h/a), the ratio of ceramic thickness to backing thickness (t_c/t_b), and the ratio of backing thickness to total thickness (t_b/h). These last two design parameters are directly related.

$$(t_c/t_b) = \frac{1-(t_b/h)}{(t_b/h)}$$

Two parameters describe the hinge: the ratio of hinge thickness to backing thickness (t_h/t_b), and the ratio of hinge radius to disc radius (r_h/a). The final design parameter is the ratio of the bender acoustical compliance (including both the disc and hinge) to the acoustical compliance of the pressure compensation cavity, (C_{DH}/C_T). The tradeoff data presented will show how the bender hydrophone performance is changed as these nondimensional design parameters are varied.

Practical design considerations place general limits on these parameters. The disc thickness parameter (h/a) can generally be limited to a range from 0.03 to 0.3. Hydrophones designed with (h/a) below this range will be very thin and have high sensitivity and capacitance, with low resonant frequency, very shallow operating depth air backed, and will be very difficult to pressure compensate. With (h/a) above this range the hydrophone will have the opposite characteristics from above and have its performance further compromised by the effects of shear displacement. Physically the parameter (t_b/h) is limited to the range from 0.0 to 1.0, i.e., no backing to no ceramic. For the trilaminar geometry the no backing case, (t_b/h) = 0 or (t_c/t_b) = ∞, is of interest since this gives a symmetrical bilaminar or bimorph hydrophone. Cases where (t_b/h) approaches 1.0 are of little interest because the hydrophone would have very little ceramic material. The range of general interest for the trilaminar geometry is from 0.0 to about 0.75 for (t_b/h) or ∞ to 0.33 for (t_c/t_b). For the bilaminar geometry these ranges are from 0.20 to 0.75 for (t_b/h) or 4.00 to .33 for (t_c/t_b). Limits on the hinge parameters can similarily be defined.

The range of interest for the pressure compensation parameter (C_{DH}/C_T) is from 0.1 to 1.0, and is set as much by performance as by physical considerations.

Four basic performance parameters are defined for the bender hydrophones considered here: the low frequency, open-circuited receiving sensitivity, $(Me)_h$, (designated as M for this report); the low frequency electrical capacitance, C_{LOW}; the short-circuited, unloaded resonant frequency, f_R^E, (designated here as f_R); and the maximum operating depth, D, (assuming a safety factor of about two for the ceramic material). The usable bandwidth of the hydrophone will be some fraction of the unloaded resonant frequency which should be chosen by the designer. The change in sensitivity will be about 3 dB between 0.5 and 0.6 f_R and will be 1 dB at about 0.4 f_R.

A nondimensional performance parameter (T_h/T) is defined which relates the maximum tensile stress in the hinge to the maximum compressive stress in the ceramic of a bilaminar disc or the maximum tensile stress in the ceramic or a trilaminar disc. With a good grade of steel as the backing and hinge material acceptable values of this parameter can be as high as 20. for the trilaminar geometry and 2.0 for the bilaminar geometry. When high strength steel is used, these numbers can be increased by 50% to 30. and 3.0.

2.2 IDEALIZED SIMPLY SUPPORTED AIR-BACKED BENDER HYDROPHONES

A useful set of basic design curves can be generated assuming the bender hydrophone has an ideal simply supported edge. These curves are presented in parametric form using the two design parameters for the disc: (h/a) and (t_c/t_b) or (t_b/h). The effects of adding physically realizable edge support and pressure compensation are then expressed as changes from these idealized design curves.

The parameter (h/a) is very useful for the design bender hydrophones. Using it, a family of hydrophones can be generated, each having the same sensitivity, resonant frequency, or impedance, etc. Thus a large thick bender hydrophone can have the same sensitivity as a small thin hydrophone, but the other performance parameters of these two hydrophone will differ greatly. This gives the designer a great deal of flexibility in specifying his design to meet particular performance goals.

2.2.1 Basic Design Curves

Figures 2.2 through 2.5 present basic design curves which were derived using the mathematical model for flexural mode transducers developed at Hydroacoustics Inc. under contracts N00140-71-C-0081 and N00024-72-C-1295. This mathematical model predicts the static and dynamic stress and performance of a general flexing disc with radial symmetry, axisymmetric load, and sinusoidal excitation. This model allows for changes in material thickness and properties as a function of radius and does not rely on a neutral stress plane concept. Very general edge conditions for a flexural mode transducer can be readily incorporated. This model also includes an approximation for the shear deflection which becomes important for thicker discs (thickness approaching one quarter the radius).

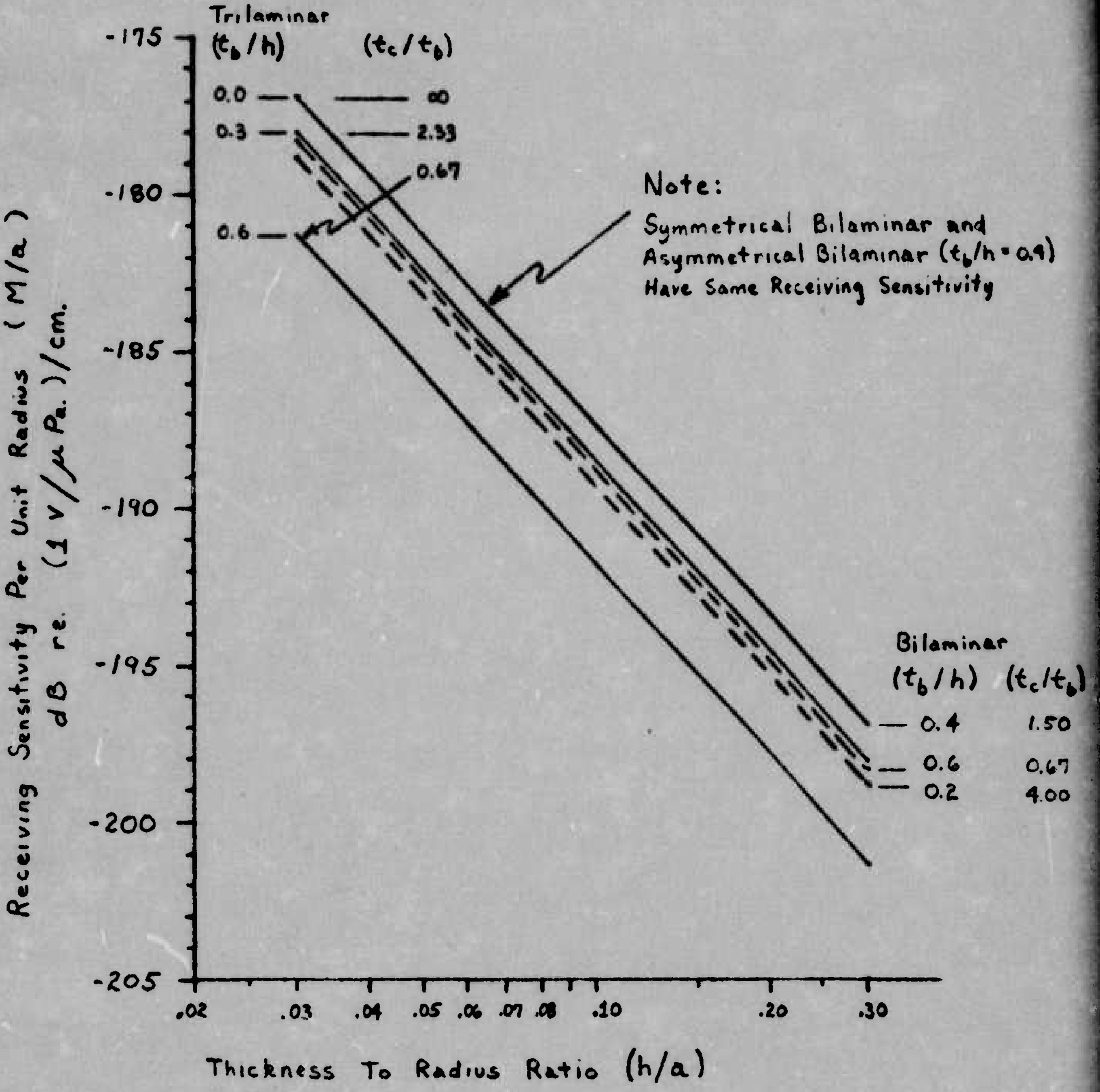

Figure 2.2 Receiving Sensitivity per unit radius for bilaminar and trilaminar bender hydrophones with PZT5A ceramic and steel backing.

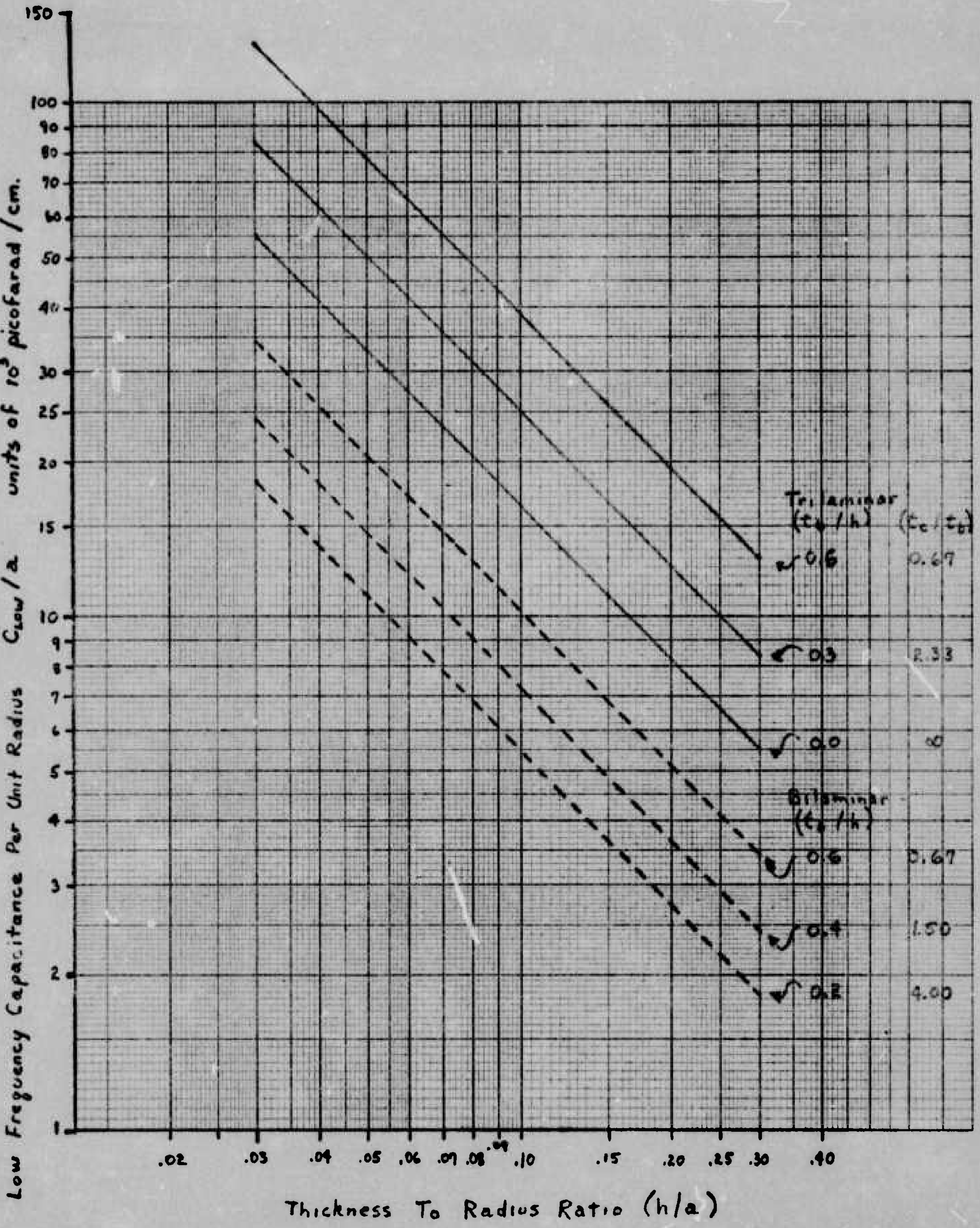

Figure 2.3 Low frequency capacitance per unit radius for bilaminar and trilaminar bender hydrophones with PZT5A ceramic and steel backing.

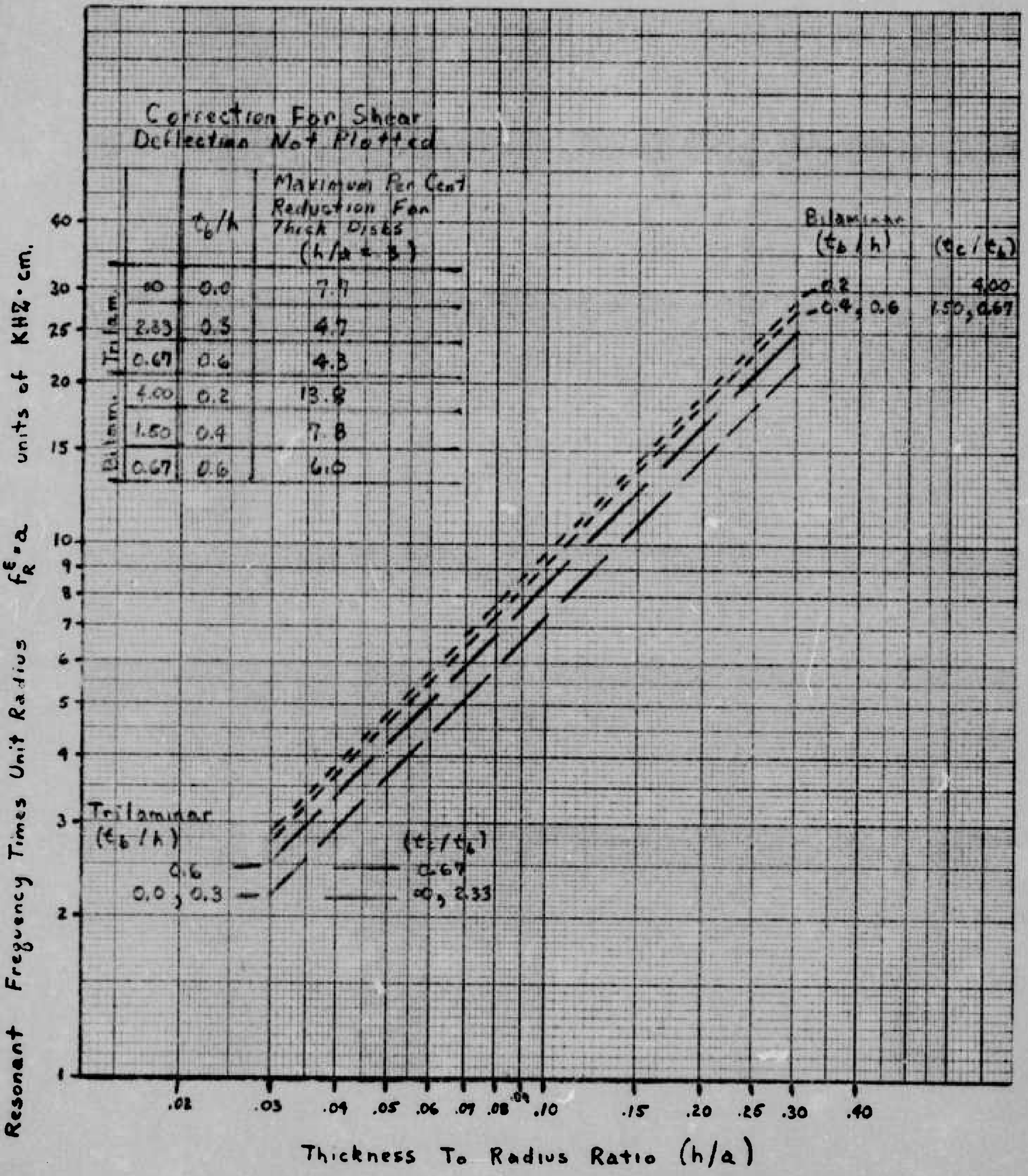

		t_b/h	Maximum Per Cent Reduction For Thick Disks (h/a = .3)
Trilam.	∞	0.0	7.9
	2.33	0.5	4.7
	0.67	0.6	4.3
Bilam.	4.00	0.2	13.8
	1.50	0.4	7.8
	0.67	0.6	6.0

Figure 2.4 Open circuit, unloaded resonant frequency times radius for bilaminar and trilaminar bender hydrophones with PZT5A ceramic and steel backing.

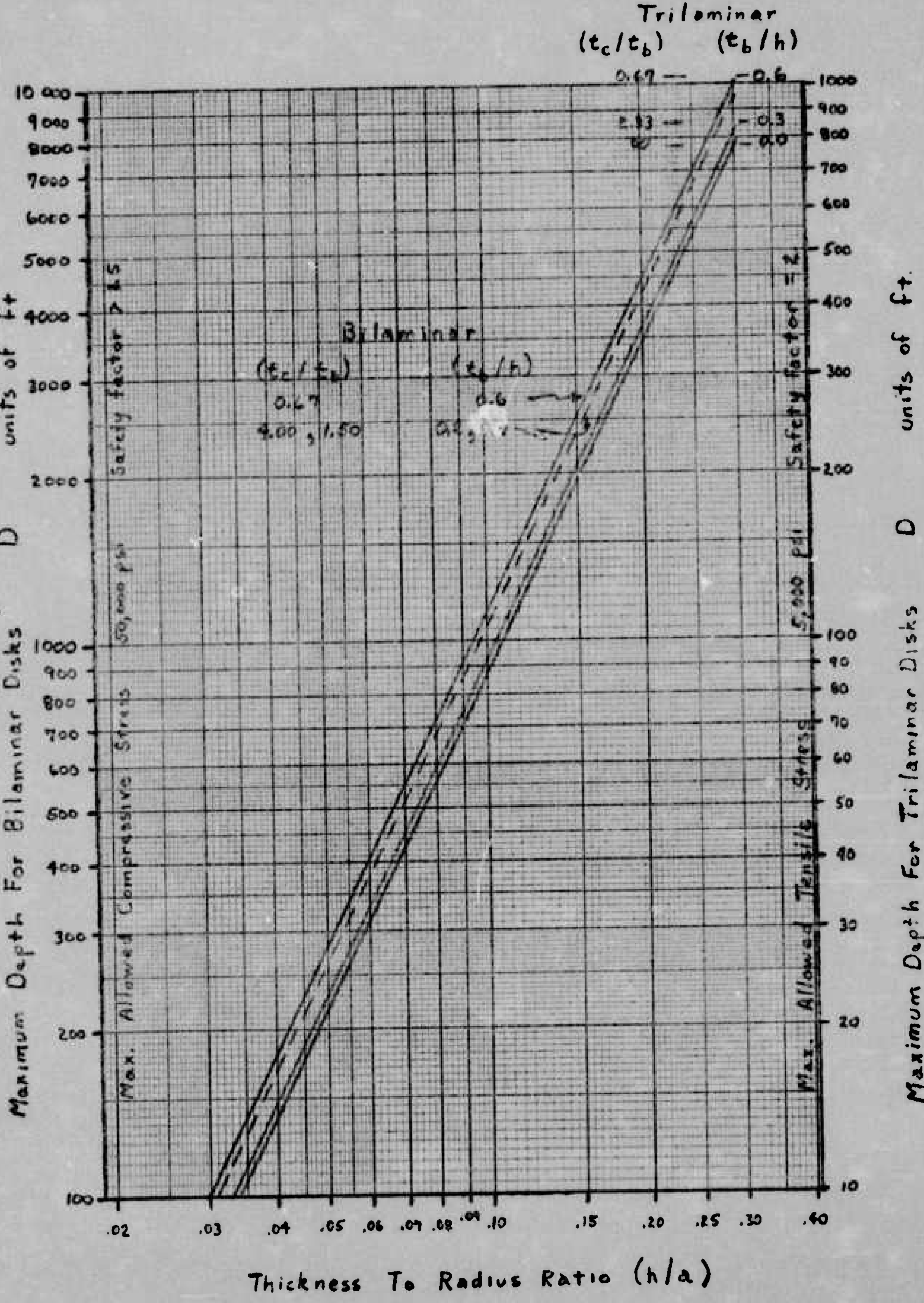

Figure 2.5 Estimated maximum depth for bilaminar and trilaminar bender hydrophones with PZT5A ceramic and steel backing.

The data presented in Figures 2.2 through 2.5 are for a steel backed hydrophone with PZT-5A ceramic. The material properties used are shown in Table 2.2. The equations in Section 2.2.3 show how to modify these curves for changes in ceramic or backing material. The performance parameters shown here are the same as those defined in Section 2.0.

Figure 2.2 shows that the receiving sensitivity* per unit radius is inversely proportional to (h/a). This curve also shows that the symmetrical bilaminar and asymmetrical bilaminar with $(t_b/h) = .4$ or $(t_c/t_b) = 1.5$ have the highest sensitivity. Changing (t_b/h) reduces M/a by as much as 4 dB for the range of parameters shown here. Changing from steel to brass or aluminum backing material changes M/a by less than 2 dB.

Figure 2.3 shows that the low frequency capacitance per unit radius for the trilaminar hydrophones* is about 4 times higher than that for the bilaminar configuration and that it is inversely proportional to (h/a). Changing parameters (t_b/h) or (t_c/t_b) over the ranges considered here changes C_{LOW}/a by about 6 dB. Switching from steel to either brass or aluminum has a negligible effect on C_{LOW}/a.

*The data in Figures 2.2 and 2.3 for the trilaminar hydrophones assume that the ceramic discs are wired in parallel. If the discs were wired in series, the receiving sensitivity would increase by 6 dB and the low frequency capacitance would decrease (increasing the impedance) by a factor of 4.

Table 2.2

Properties of the Materials used in the Bender Hydrophone Study.

	Kg/M^3	S_{11}^D M^2/N	S_{12}^D M^2/N	S_{44}^D M^2/N	g_{31} V-M/N	ε_{33}^T farads/M
PZT-5A	7750	$1.440 \cdot 10^{-11}$	$-7.710 \cdot 10^{-12}$	$2.520 \cdot 10^{-11}$	$-1.140 \cdot 10^{-02}$	$+1.505 \cdot 10^{-8}$
Steel	7860	$4.830 \cdot 10^{-12}$	$-1.600 \cdot 10^{-12}$	$1.286 \cdot 10^{-11}$	0.0	0.0
Brass	8514	$9.662 \cdot 10^{-12}$	$-3.188 \cdot 10^{-12}$	$2.570 \cdot 10^{-11}$	0.0	0.0
Aluminum	2713	$1.450 \cdot 10^{-11}$	$-4.785 \cdot 10^{-12}$	$3.857 \cdot 10^{-11}$	0.0	0.0

Figure 2.4 shows that the open circuit, unloaded resonant frequency times radius is proportional to the parameter (h/a) and does not significantly change as (t_b/h) or (t_c/t_b) is changed. The effect of shear in the thicker discs (h/a equal to .3) reduced $f_{R*}a$ by 5 to 15% depending on the configuration and value of (t_b/h) or (t_c/t_b). Changing from steel to brass can reduce $f_{R*}a$ by as much as 15% while changing from steel to aluminum can change $f_{R*}a$ by as much as ±10% depending upon the configurations.

Figure 2.5 shows that changing the parameters (t_b/h) or (t_c/t_b) has a small effect on the maximum depth: 5% for the range shown for bilaminar benders and 25% for trilaminar benders. The maximum depth shown here is calculated from the maximum radial stress produced in the ceramic by a uniform hydrostatic pressure on one side of the bender. A safety factor of about two has been assumed in specifying the maximum depth.[5] Because the asymmetrical bilaminar bender has ceramic on only one surface, it can be assembled so that a hydrostatic load produces only compressive stress in the ceramic. This gives a factor of ten increase in operating depth over the trilaminar configuration. This is reflected in Figure 2.5 by two vertical scales: one for bilaminar and one for trilaminar benders.

2.2.2 Combined Performance Parameters

It is possible to define many combinations of the four performance parameters shown in Figures 2.2 through 2.5 which are independent of the parameter (h/a) and depend only on the parameter (t_b/h) or (t_c/t_b). Three such combinations are described below.

$$C_1 = M * f_R$$

$$C_2 = M / C_{LOW}$$

$$C_3 = M * C_{LOW} * D / a^2$$

If one performance parameter is held constant, these combinations of parameters may be used to show the trade-off relationships for the remaining parameters as shown in Table 2.3.

Table 2.4 gives the values of the three combination parameters for various values of (t_b/h) and (t_c/t_b) for both bilaminar and trilaminar benders. All three of these parameters go to zero as (t_b/h) approaches zero for the bilaminar benders and go to zero as (t_b/h) approaches one for both bilaminar and trilaminar benders.

The parameter C_1 for asymmetrical assemblies is up to 33% higher than that for trilaminar benders with the same proportion of metal backing (t_b/h). An optimum value of (t_b/h) exists for asymmetrical benders whereas this product decreases monotonically for increasing (t_b/h) of trilaminar assemblies.

Bilaminar assemblies have values of C_2 which are approximately 4 times that of corresponding trilaminar assemblies. Although M values are almost equal for comparable bilaminar and trilaminar assemblies, the values of C_{LOW} are not. Parameter C_2 has a maximum value near (t_b/h) equal to .2, (t_c/t_b) equal to 4., for bilaminar benders. No such peak exists for the trilaminar configuration.

Table 2.3

Design Tradeoff Parameters For One Performance Parameter Fixed.

	Design Criteria			
Performance Parameter	Fixed Depth	Fixed Sensitivity	Fixed Capacitance	Fixed Bandwidth
D	D	$\left(\frac{a}{M}\right)^2 C_2 C_3$	$\left(\frac{a}{C_{LOW}}\right)^2 \frac{C_3}{C_2}$	$\left(\frac{a f_R}{C_1}\right)^2 C_2 C_3$
M	$a\sqrt{\frac{C_2 C_3}{D}}$	M	$C_2 \times C_{LOW}$	$\frac{C_1}{f_R}$
C_{LOW}	$a\sqrt{\frac{C_3}{C_2 D}}$	$\frac{M}{C_2}$	C_{LOW}	$\frac{C_1}{C_2 f_R}$
f_R	$\frac{C_1}{a}\sqrt{\frac{D}{C_2 C_3}}$	$\frac{C_1}{M}$	$\frac{C_1}{C_2 C_{LOW}}$	f_R

Table 2.4

Combined Parameters for Bilaminar and Trilaminar Bender Hydrophones with PZT-5A Ceramic and Steel Backing

Trilaminar(1)

t_c/t_b	t_b/h	C_1	C_2	C_3
∞	0.0	31.5	0.259	6.17
2.33	0.3	27.5	0.151	8.68
0.67	0.6	18.8	0.057	10.33
0.00	1.0	0.0	0.0	0.0

Bilaminar

t_c/t_b	t_b/h	C_1	C_2	C_3
∞	0.0	0.0	0.0	0.0
4.00	0.2	32.7	0.624	20.0
1.50	0.4	39.2	0.585	32.9
0.67	0.6	33.8	0.356	42.8
0.00	1.00	0.0	0.0	0.0

$C_1 = M * f_R$ $10^{-10} *$ KHz * V/ µPa

$C_2 = M / C_{LOW}$ $10^{-13} *$ V/(µPa * pfd)

$C_3 = M * C_{LOW} * D / a^2$ $10^{-4} *$ V * pfd * ft/(µPa * cm^2)

(1) The data for the trilaminar hydrophones assume that the ceramic discs are wired in parallel. If the discs are wired in series, the sensitivity would increase by 6 dB and the low frequency capacitance would decrease by a factor of 4.

The parameter C_3 shows that in general sensitivity must be traded off for depth unless capacitance can be reduced. Parameter C_3 is greater for bilaminar assemblies because of their greater depth capability when assembled to be compressively stressed by hydrostatic pressure. This parameter has a maximum value above (t_b/h) equal to .6, (t_c/t_b) equal to .67, for both the bilaminar and trilaminar benders.

2.2.3 Equations to Account for Material Changes

This section presents equations which can be used to approximate the change in performance parameters when either the ceramic or backing material properties are changed. These equations are simplified where possible and use the nomenclature defined in Table 2.1. One simplification is made with respect to the Poisson ratio for the backing and ceramic. For most metals of interest σ^b is approximately 0.3, and for most ceramics used in hydrophones σ^D is approximately 0.5. Parameters which are weak functions of the Poisson ratio use these approximations.

2.2.3.1 Symmetrical Trilaminar Equations

The equations for the performance parameters of a symmetrical trilaminar bender hydrophone are directly related to the assumed normalized deflection curve of the bender. These equations are developed from the closed form solution of a symmetrical trilaminar bender. Four coefficients can be defined which are independent of this deflection curve; five other coefficients must be evaluated as a function of the bender shape.

$$k_p^2 = \frac{2\, g_{31}^2}{2\, g_{31}^2 + S_{11}^D(1 - \sigma^D)/\varepsilon_{33}^T}$$

$$C_b = 4A(1 - k_p^2)\varepsilon_{33}^T/t_c$$

$$\tau_1 = \frac{(h + t_b)^2}{h^2 + t_b h + t_b^2}$$

$$\bar{\rho} = \frac{\rho_b t_b + \rho_c t_c}{h}$$

For voltage parameters M, and C_{LOW}, the assumed normalized deflection curve is

$$Y_N = 1 - \left(r/_a\right)^2$$

which is the curve for an applied edge moment. Because of its simplicity, this curve is also used to approximate the maximum radial stress which in turn is used to estimate the maximum depth. The following five coefficients were developed using this deflection curve.

$$N = 2\pi\, k_p(h + t_b)\left(\frac{2(1 - k_p^2)\varepsilon_{33}^T}{S_{11}^D\,(1 - \sigma^D)}\right)^{1/2}$$

$$\Lambda^b = \frac{1 + \sigma^b}{2} \doteq .65$$

$$\Lambda^D = \frac{1 + \sigma^D}{2} \doteq .75$$

$$\Lambda^E = \Lambda^D - .375\, k_p^2(1-\sigma^D)\alpha_1$$

$$\Lambda^E \doteq .75\left[1 - .25\, k_p^2\, \alpha_1\right]$$

$$\zeta = \frac{16\pi}{3a^2}\left[\frac{\Lambda^E(h^3 - t_b^3)}{S_{11}^D\left(1 - \sigma^{D^2}\right)} + \frac{\Lambda^b E^b t_b^3}{\left(1 - \sigma^{b^2}\right)}\right]$$

$$\zeta \doteq \frac{16.8}{a^2}\left[\frac{1.33\, \Lambda^E(h^3 - t_b^3)}{S_{11}^D} + .72\, E^b t_b^3\right]$$

$$\boxed{C_{LOW} = C_b + N^2/\zeta}$$

$$\boxed{M = \frac{NA}{C_{LOW}}}$$

$$\boxed{T \doteq \frac{1.67\, h}{S_{11}^D}}$$

The deflection equation used to calculate the short circuit, unloaded resonant frequency is

$$Y_n = 1 - 1.4417\left(\frac{r}{a}\right)^2 + .3304\left(\frac{r}{a}\right)^3 + .1112\left(\frac{r}{a}\right)^4$$

and the following coefficients are defined.

$$\Lambda^{b} = .353 + .262\ \sigma^{b} \doteq .432$$

$$\Lambda^{D} = .353 + .262\ \sigma^{D} \doteq .484$$

$$\Lambda^{E} = \Lambda^{D} - .231\ k_p^2\ (1 - \sigma^{D})\kappa_1 \doteq .484 - .116\ k_p^2\ \kappa_1$$

$$\zeta = \frac{16\pi}{3a^2}\left[\frac{\Lambda^{E}(h^3 - t_b^3)}{S_{11}^{D}\left(1 - \sigma^{D^2}\right)} + \frac{\Lambda^{b}E^{b}t_b^3}{\left(1 - \sigma^{b^2}\right)}\right]$$

$$\zeta \doteq \frac{16.8}{a^2}\left[\frac{1.33\Lambda^{E}(h^3 - t_b^3)}{S_{11}^{D}} + .48\ E^{b}t_b^3\right]$$

$$\boxed{f_R = \frac{.084}{a}\left(\frac{\zeta}{\bar{\rho}\,h}\right)^{1/2}}$$

2.2.3.2 Asymmetrical Bilaminar Equation

A simple neutral stress plane development of the model for asymmetrical bilaminar discs does not yield satisfactory prediction accuracy. The following equations have been empirically developed from the computer model predictions to predict the approximate performance for the t_b/h ratio which gives the maximum receiving sensitivity.

A coordinate of the mechanical neutral stress plane, t_n, has proven to be a useful parameter in locating the near optimum ratio of ceramic to metal thickness and is defined below.

$$t_n = \frac{h}{2}\left[\frac{t_b}{h} - \frac{(h - t_b)}{\left(\frac{E^b}{E^c} - 1\right) t_b}\right]$$

A positive value of t_n means that this plane is in the backing material; a negative value places it in the ceramic. The optimum value of t_b/h is slightly greater than or equal to that obtained when $t_n = 0.0$.

$$\left(t_b/h\right)\text{opt.} \geqslant \frac{\sqrt{E^b/E^c} - 1}{\left(E^b/E^c - 1\right)}$$

The approximate equations for the performance parameters for this value of t_b/h are given below.

$$k_p^2 = \frac{2\, g_{31}^2}{2\, g_{31}^2 + s_{11}^D(1 - \sigma^D)/\varepsilon_{33}^T}$$

$$C_b = A(1 - k_p^2)\,\varepsilon_{33}^T/t_c$$

$$\boxed{C_{LOW} \doteq 1.47\, C_b}$$

$$\boxed{M \doteq \frac{.975 \times 10^{-7}\, a^2}{h\, k_p}\left[\frac{s_{11}^D\,(1 - \sigma^D)}{\varepsilon_{33}^T\,(1 - k_p^2)}\right]^{1/2}}$$

$$\bar{E} = \frac{E^{b}\left[(t_b - t_n)^3\right] + E^{c}\left[(t_c + t_n)^3 - t_n{}^3\right]}{(t_c + t_n)^3 + (t_b - t_n)^3}$$

$$\boxed{T \doteq \frac{1.5\ E^{c}a^2}{\bar{E}\ h^2}}$$

$$\bar{\rho} = \frac{\rho_b t_b + \rho_c t_c}{h}$$

$$\bar{\sigma} = \frac{\sigma^{b} t_b + \sigma^{E} t_c}{h}$$

$$\boxed{f_R \doteq \frac{.233\ h}{a^2}\left(\frac{\bar{E}}{\bar{\rho}\,(1 - \bar{\sigma}^2)}\right)^{1/2}}$$

2.3 AIR-BACKED HYDROPHONE WITH HINGE EDGE SUPPORT

In the previous section computer generated design trade off curves for bender hydrophones were presented as functions of two non-dimensional parameters: (h/a), total bender thickness to radius ratio, and (t_c/t_b), ceramic thickness to backing thickness ratio. A third parameter (t_b/h) which is directly related to (t_c/t_b) was also shown. This data assumed the simplest bender hydrophone geometry: a bender with uniform thickness for both the backing and ceramic material and an ideal simply supported edge. The performance parameters used for these curves are open circuit receiving sensitivity, M; low frequency electrical capacitance, C_{LOW}; short-circuited, unloaded resonant frequency, f_R; and maximum depth, D. The effect on these parameters of adding a simple hinge to the bender hydrophone is now examined.

2.3.1 Simple Uniform Hinge

A sketch of the composite bender and hinge to be considered here was shown in Figure 1 in Section 2.0. Two non-dimensional parameters are used to describe the hinge: (t_h/t_b), hinge thickness to backing thickness ratio; and (r_h/a), hinge radius to ceramic radius ratio. One additional performance parameter has been introduced to describe the stress in the hinge: $(r_h/a\ )$, maximum radial hinge stress to maximum radial ceramic stress ratio. Most backing materials can support twice the compressive stress and twenty times the tensile stress possible for the ceramics used.

The maximum radial bending stress in the hinge is strongly dependent on the hinge thickness. For a uniform static pressure this stress is roughly proportional to $t_h^{-1.6}$ for (t_h/t_b) between 0.25 and 1.0 (for trilaminar bender parameters $(h/a) = 0.03$ and $(t_c/t_b) = 2.33$). This stress would be proportional to t_h^{-2}. for an ideal clamped-clamped ring.

When a simple hinge like that shown in Figure 2.1 is used instead of an ideal simple support, the parameters M, C_{LOW}, f_R, and D change as shown in Tables 2.5 and 2.6. These results apply to any value of the relative thickness parameter (h/a) except for f_R for which the change factor is valid for thin hinges but is only an approximation for thicker hinges because of the effects of shear.

These tables are used with the four basic design trade off curves presented in the previous section. To assess the effect of adding a simple hinge to a bender hydrophone, multiply any of the performance parameters M, C_{LOW}, f_R, or D by the appropriate factor shown in this table. The last entry in this table shows the ratio of hinge to ceramic stress. As mentioned earlier, values of this parameter greater than 2.0 for bilaminar and 20.0 for trilaminar hydrophones may give a design in which the hinge stresses limit the operating depth. All of the bilaminar hydrophone designs shown here have a stress ratio greater than 2.0 although some of them are close enough to be considered. (Materials with an ultimate tensile strength greater that 200K psi would be required for the backing material.)

Table 2.5

Changes in Performance Parameters When A Simple Hinge Replaces the Ideal Support for Air Backed, Bilaminar, Bender Hydrophones

		$r_h/a = 1.10$			$r_h/a = 1.20$	
	(t_h/t_b)	1.00	.75	.50	1.00	.50
	(t_c/t_b)					
M	4.00	1.50	1.53	1.52	1.78	1.74
	1.50	.885	1.09	1.24	1.23	1.50
	.67	.426	.695	1.03	.750	1.35
	.33	.251	.470	.848	-	-
C_{LOW}	4.00	.962	.972	.979	.973	.984
	1.50	.872	.926	.970	.918	.982
	.67	.807	.857	.928	.843	.956
	.33	.848	.874	.924	-	-
f_R	4.00	.929	.888	.788	.759	.421
	1.50	1.04	.958	.887	.914	.727
	.67	1.22	1.08	.931	1.08	.797
	.33	1.31	1.16	.968	-	-
D	4.00	1.07	1.05	1.02	.942	.900
	1.50	1.19	1.06	.986	.988	.863
	.67	1.56	1.27	1.03	1.22	.864
	.33	1.91	1.52	1.12	-	-
T_h/T	4.00	2.37	3.59	7.71	5.32	20.3
	1.50	2.19	2.11	2.51	2.22	5.10
	.67	2.70	2.77	2.62	2.33	3.05
	.33	3.03	3.44	3.36	-	-

Table 2.6

Changes in Performance Parameters When A Simple Hinge Replaces the Ideal Support for Air Backed, Trilaminar, Bender Hydrophones

		$r_h/a = 1.10$		$r_h/a = 1.20$	
	(t_h/t_b)	1.0	0.5	1.0	0.5
	(t_c/t_b)				
M	2.33	.851	1.15	1.19	1.40
	.67	-	-	-	1.22
C_{LOW}	2.33	.879	.978	.924	.988
	.67	-	-	-	.957
f_R	2.33	.994	.833	.822	.655
	.67	-	-	-	.797
D	2.33	1.09	.924	.906	.817
	.67	-	-	-	.882
T_h/T	2.33	3.26	4.36	3.36	8.07
	.67	-	-	-	4.03

These results show that thin hinges with larger values of (r_h/a) would be preferred if the stress criterion can be met. In general these hinges would slightly increase the hydrophone sensitivity over an ideal simple edge support and have a small effect on the other parameters.

The low frequency capacitance, C_{LOW}, is always reduced by the addition of a simple hinge. The resonance frequency f_R was also reduced for most of the hinge configurations tested. The results also show that in general the depth limit, D, of the air backed bender hydrophone is reduced with a clamped hinge design. Increases in the depth capability of the hydrophone gained by the addition of a simple hinge are always accompanied by a reduction in the sensitivity. Table 6 is a much abbreviated version of Table 5 but shows the same trends for the trilaminar bender hydrophone as seen for the bilaminar geometry.

2.3.2 Tapered Web Hinge

One practical means of approximating a simple uniform hinge is shown in Figure 2.6 where a flexible edge support is achieved by a smoothly tapered web. The performance of this hinge is determined using Table 2.7 and Figures 2.2 through 2.5 in a way similar to that described in the previous section. Each change factor relates the performance of a hydrophone with this web-type hinge to the comparable hydrophone with an ideal simple edge support.

TABLE 2.7

CHANGES IN PERFORMANCE PARAMETERS WHEN A WEB-TYPE HINGE REPLACES THE IDEAL SIMPLE SUPPORT FOR AIR-BACKED, BILAMINAR, BENDER HYDROPHONES

	$r_h/a = 1.10$			
t_h/t_b	.50	.25	.125	.0625
M	1.10	1.21	1.23	1.22
C_{LOW}	.940	.982	.991	.994
f_R	.956	.899	.860	.797
D	1.06	.998	.979	.970
T_h/T	11.7	12.5	12.7	12.8

$t_c/t_b = 1.50$ for all hinges.

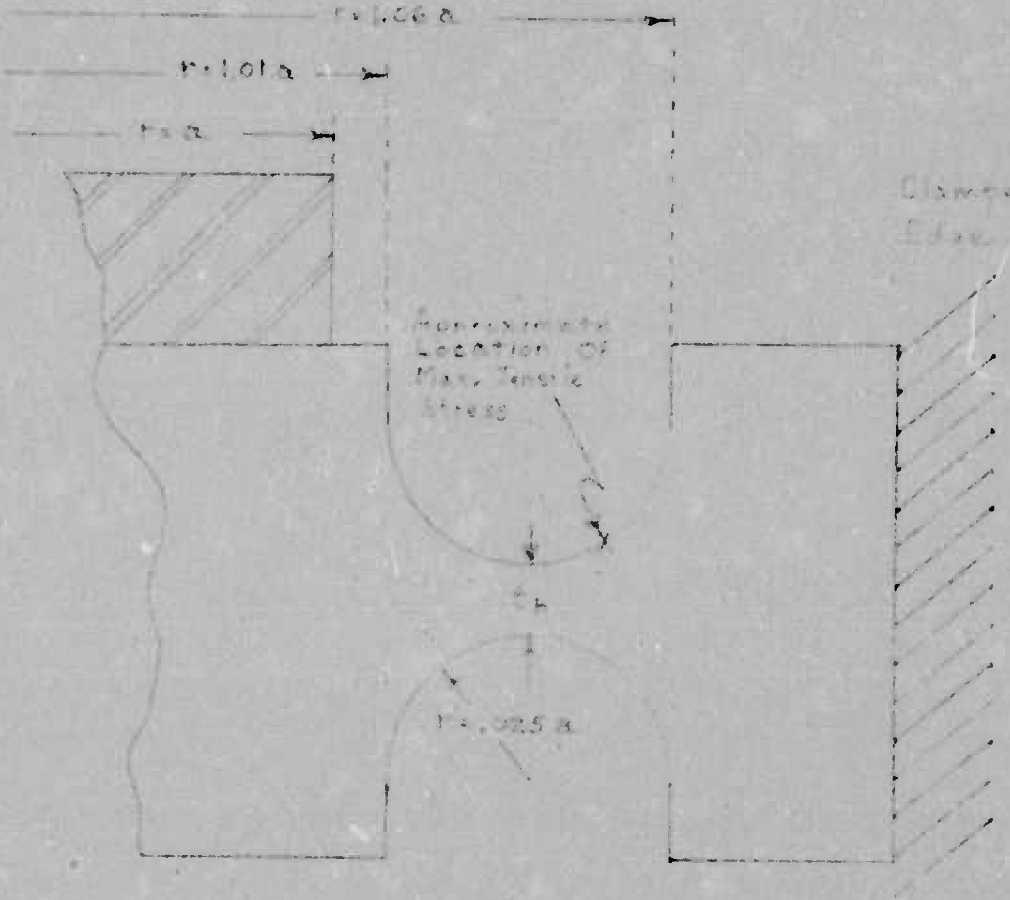

Figure 2.6 Geometry and Dimensions of Tapered Web Hinge

For this study the ratio of minimum hinge thickness to back material thickness (t_h/t_b) was varied from 0.5 to 0.0625. The performance with this web hinge design is about the same as that found for a simple uniform hinge. The data shows a slight reduction in the stress ratio (T_h/T), but it is possible that the true maximum stress was not found in the web hinge. The region of highest tensile stress occurs at a radius midway between the radius of minimum and maximum thickness in the clamped edge side of the hinge. The stress data shows that webs as thin as 0.125 t_b probably are not useful.

2.4 PRESSURE-COMPENSATED HYDROPHONE WITH SIMPLE HINGE EDGE SUPPORT

The hydrophones described up to this point have been limited to relatively shallow water (down to several thousand feet). Many applications require operation in water with depths greatly exceeding 2000 feet. The hydrostatic pressure at these depths will fracture the disc unless some form of pressure compensation is provided. Since the performance of a bender hydrophone can be affected by the impedance of the terminating cavity, an additional design compromise must be made between the hydrophone size and its acoustic performance.

The most likely (and at first appearances, best) choice would be to fill the terminating cavity with a gas which is maintained at the same pressure as the ambient hydrostatic pressure. Unfortunately such pressure compensation systems have proven to be unreliable and quite bulky making it necessary to go to a liquid filled pressure compensation cavity. A liquid with high compressibility (like silicone oil) can be used in the cavity, and a pressure equalizing system with high acoustic impedance (a long, small diameter hole) can be used to compensate for the hydrostatic pressure. This section treats such a pressure compensation system for bender hydrophones.

The liquid filled cavity will change the acoustic performance of the hydrophone by adding stiffness which increases the resonant frequency, decreases the receiving sensitivity, and decreases the low frequency capacitance. The change in low frequency capacitance is small and can be neglected entirely for suitable cavity compliance.

The acoustic impedance of the pressure equalizing passage will introduce a low frequency roll off to the hydrophone frequency response. The compliance of the terminating cavity, C_T, is given by $C_T = V/\beta$, where V is the volume of the liquid filled cavity and β is the bulk modulus of the liquid. The roll-off frequency is given by

$$f_{LOW} = \frac{1}{2\pi\sqrt{L_P C_T}}$$

where L_P is the passage inertance which compensates for the hydrostatic pressure. This roll-off can be made to start at an arbitrarily low frequency by adjusting the passage inertance (changing the area and length).

The effect of the liquid filled cavity on the hydrophone performance can be described using the ratio of the compliance of the air-backed, composite disc-hinge, C_{DH}, to the compliance of the terminating cavity, C_T. The liquid backed, pressure compensated hydrophones of most interest have C_{DH} less than $3*C_T$ or the terminating cavity is less than three times as stiff as the composite disc-hinge. The sensitivity and resonant frequency of these pressure compensated hydrophones, M_{PC} and F_{RPC}, are related to the air backed sensitivity and resonant frequency by the following relationships.

$$M_{PC} = M\left(\frac{1}{1 + C_{DH}/C_T}\right)$$

$$f_{PRC} = f_R\left(1 + C_{DH}/C_T\right)^{1/2}$$

The values for M and f_R are obtained using the procedures outlined in Sections 2.2 and 2.3. As can be seen in these two equations, the sensitivity-bandwidth product for a pressure compensated hydrophone is always less than the product for the same hydrophone air-backed. To minimize the effect of liquid backing, large liquid compliances are desirable. The compliance C_T is proportional to the cavity volume and is, therefore, limited by the physical size the designer is willing to use. The cavity volume is also limited by the highest frequency to be measured since the cavity dimensions should be a small fraction of a wavelength.

A satisfactory liquid compensated hydrophone is not necessarily obtained by simply adding a liquid cavity to a good air-backed hydrophone. A sensitive air-backed bender hydrophone will generally have a small (h/a) ratio and be limited to quite shallow operation. When this hydrophone is liquid backed to provide pressure compensation, the results are discouraging at best because a very large pressure compensation cavity is required. Since the basic compliance of a disc is inversely proportional to the ratio (h/a) cubed, thicker discs can use much more reasonable liquid compensation cavities. One disadvantage in using thick discs is the added displacement due to shear which can increase the compliance of the hinge and disc by as much as 40%. The optimum value of (h/a) seems to be near 0.1 where the increase in sensitivity for a thinner disc is off set by the reduction in sensitivity due to liquid backing and the shear displacement is not significant. For these reasons thicker discs with stiffer hinges are more suited for pressure compensation than thin discs or flexible hinges.

Table 2.8 lists the acoustical complance for several combinations of the discs and hinges considered earlier. This table shows the importance of the hinge when a hydrophone is pressure compensated using liquid backing. In Section 2.3, it was shown that adding a properly designed hinge to a disc has a small effect on the hydrophone performance parameters. Adding a hinge to a disc does make a significant change in the compliance of the composite disc-hinge. A two to one change in C_{DH} such as shown in this table will require a two to one change in the volume of the pressure compensation cavity. The data shown here are for bilaminar discs with a radius of 0.01 M (1 cm) and a thickness ratio (h/a) of 0.3. In order to use this table for other values of a or (h/a) the following relationship should be used.

$$C_{DH}(a,\ h/a) = (100\ a)^3 \left(\frac{0.3}{h/a}\right)^3 \ C_{DH}(.01,\ 0.3)$$

The values of C_T(.01, 0.3) are from the table and a is in meters. Since the effect of shear displacement is included in the data for this table, the above relationship is not accurate for small values of (h/a).

Table 2.8 Acoustical Compliance of Composite Bilaminar Disc-Hinge Hydrophones using Simple, Uniform Hinges.

	t_h/t_b		
t_c/t_b	1.0	.75	.50
4.00	.423	.504	.764
1.50	.296	.348	.425
.67	.205	.268	.358
.33	.151	.184	.296

NOTES:

1. Units on compliance are 10^{-15} M^5/N
2. Disc parameters are $(h/a) = .3$ and $a = .01M$.
3. Hinge radius parameter $(r_h/a) = 1.10$
4. Hinge geometry shown in Figure 2.1.

3.0 MODELING DIRECT MODULATION OF SEA WATER FLOW

The hydraulic valve which modulates the flow between the high pressure source and low pressure sink is the heart of the hydroacoustic power oscillator. Typically it has been analyzed using Bernoulli's Equation* for the steady flow of an inviscoid, incompressible fluid.

$$\frac{P_1}{\rho} + \frac{V_1^2}{2} + gZ_1 = \frac{P_2}{\rho} + \frac{V_2^2}{2} + gZ_2$$

Where P is the pressure, V is the particle velocity, Z is the height above datum, ρ is the fluid density, and g is the acceleration due to gravity. Subscripts 1 and 2 refer to a section of fluid on opposite sides of the valve. Let subscript 1 be used for conditions in the supply reservoir where V is approximately equal to zero, and 2 be used for conditions at the exhaust of the valve which is at the same datum level as the supply reservoir ($Z_1 = Z_2$).

Bernoulli's equation reduces to

$$\frac{P_1}{\rho} = \frac{P_2}{\rho} + \frac{V_2^2}{2} \quad \text{or}$$

$$V_2^2 = \frac{2}{\rho} (P_1 - P_2)$$

This can be rewritten as

$$Q|Q| = \frac{2A^2 C_D^2}{\rho} \Delta P$$

Where Q is the volume flow rate, A is the open area of the valve, and C_D is the discharge coefficient (C_D can be as high as 1.0 for fully rounded valves, and C_D as low as 0.6 for sharp edged valves).

---

*For example, see "Fluid Power Control" by J.F. Blackburn, G. Reethof, and J.O. Shearer, John Wiley & Sons, 1960

The shape of the valve opening has very little effect on C_D; a long narrow slit has the same value as a circular hole. To reiterate, Equation 1 applies to an ideal nonviscous and incompressible fluid flow where steady-state conditions prevail. These assumptions are reasonably accurate for most hydraulic valves used in fluid power control systems but must be reexamined when considering the hydroacoustic power oscillator which operates at considerably higher frequency than most fluid power systems.

3.1 DIFFERENTIAL EQUATION FOR VALVE FLOW

Navier-Stokes equations,* which describe the conservation of momentum, constitute the fundamental basic of fluid flow theory. If it is assumed that the fluid is nonviscous or that the contribution by viscous terms in the equations is much smaller that that by the inertia terms, one can ignore the affects of viscosity. Then the equations are reduced to Euler's equations valid for an ideal fluid and are given by

$$\rho\frac{\partial\bar{v}}{\partial t} + \rho(\bar{v}\cdot\nabla)\bar{v} + \nabla P = \bar{F}$$

where ρ is the fluid density, $\bar{v}$ is the particle velocity vector, P is the fluid pressure and $\bar{F}$ is the applied force vector.

For one dimension flow this equation reduces to

$$0 = \frac{\partial P}{\partial X} + \rho\frac{\partial v}{\partial t} + \rho v\frac{\partial v}{\partial X}$$

and can be integrated along a streamline from region ① to region ② as shown in Figure 3-1.

$$0 = \int_{\textcircled{1}}^{\textcircled{2}} \frac{\partial P}{\partial X}\, ds + \int_{\textcircled{1}}^{\textcircled{2}} \frac{\partial v}{\partial t}\, ds + \int_{\textcircled{1}}^{\textcircled{2}} \frac{v\,\partial v}{\partial X}\, ds$$

$$0 = P_2 - P_1 + \rho\int_{\textcircled{1}}^{\textcircled{2}} \frac{\partial v}{\partial t}\, ds + \rho\frac{V_2^2}{2}\,(\text{sgn } v)$$

where sgn v equals 1 if v is positive and equals -1 if v is negative. The velocity in region ① is assumed to be zero, and v_2 is the discharge velocity from the orifice. The conversion from particle velocity to the volume velocity through the valve, Q_v, is given by

---

*For example, see "Mechanics of Deformable Bodies" by Arnold Sommerfeld, Academic Press, 1950.

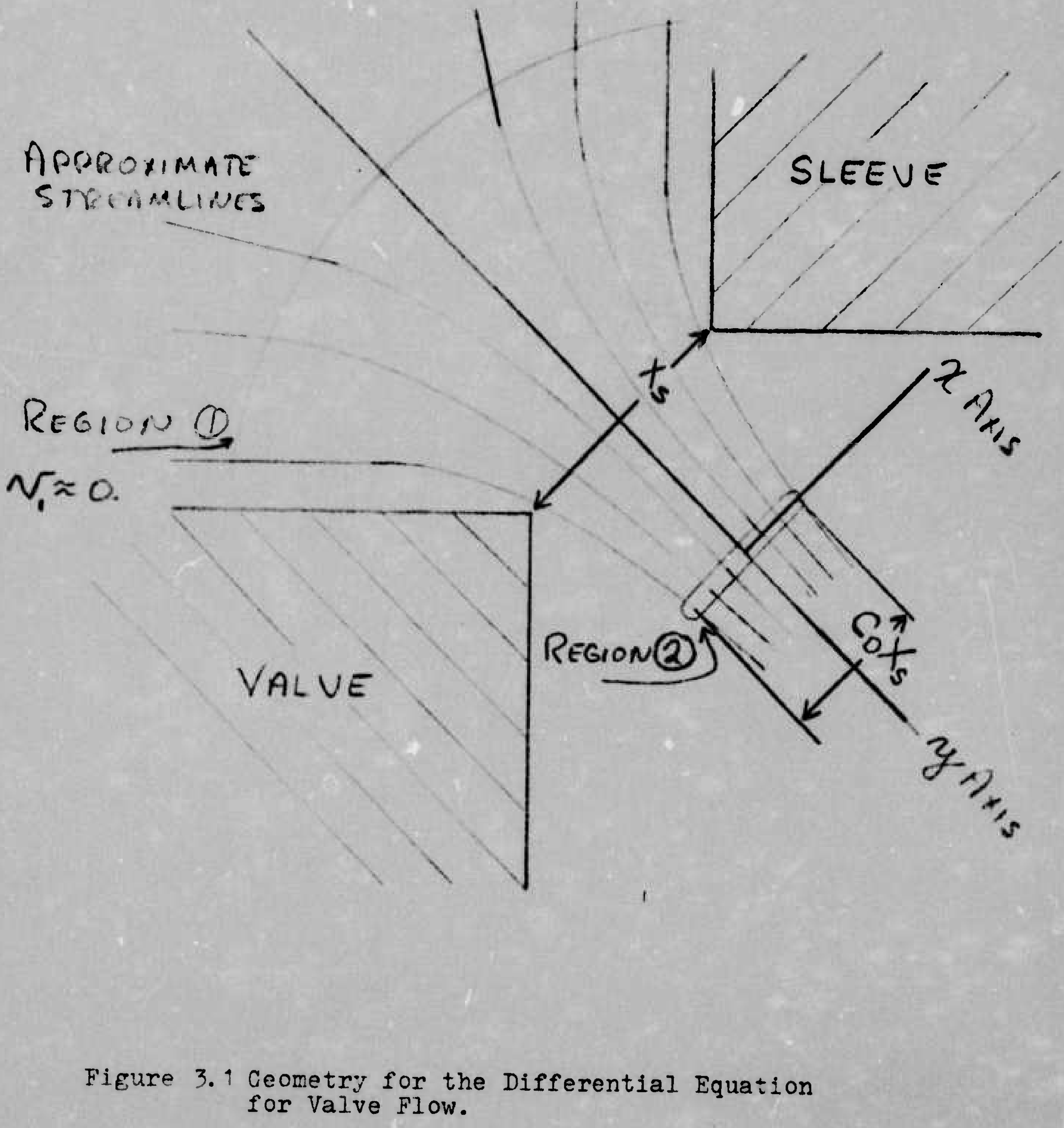

Figure 3.1 Geometry for the Differential Equation for Valve Flow.

$$v = \frac{Q_v}{KX} \text{ or } v_2 = \frac{Q_v}{K\,C_D X_S}$$

where $K = \pi * D_V * P_F$

D_V is the valve diameter

P_F is the valve porting fraction

C_D is the discharge coefficient ($C_D \doteq .6$ for sharp edged valves).

$$P_1 - P_2 = \frac{\rho Q_v^2 \operatorname{sgn}(Q_v)}{2K^2 C_D^2 X_S^2} + \frac{\rho}{K} \int_{\text{①}}^{\text{②}} \frac{\partial}{\partial t} \left[\frac{Q_v}{X_S} \right] dy$$

If one approximates the streamlines, then X can be replaced by

$$X \doteq 2 \left[\left(\frac{C_D X_S}{2} \right)^2 + y^2 \right]^{\frac{1}{2}}$$

and the last term in the previous equation becomes

$$\frac{\rho}{K} \int_{\text{①}}^{\text{②}} \frac{\partial}{\partial t} \left[\frac{Q_V}{X} \right] dy \doteq \frac{\rho}{K} \int_{\text{①}}^{\text{②}} \frac{\partial Q_V}{\partial t} \frac{dy}{2\,(C_D X_S)^2 + y^2}$$

$$- \frac{\rho}{K} \int_{\text{①}}^{\text{②}} \frac{C_D^2 \quad Q_v X_S}{8 \left[(C_D X_S)^2 + y^2 \right]^{3/2}} \frac{\partial X_S}{\partial t} dy$$

Approximate y in region 1 by $-10X_s$, by 0 in region 2, and carrying out the indicated integration gives

$$\frac{\rho}{K}\int_{\textcircled{1}}^{\textcircled{2}}\frac{\partial}{\partial t}\left[\frac{Q_v}{X_S}\right]dy \doteq \frac{\rho}{2K}\frac{\partial Q_v}{\partial t}\ln\left(\frac{C_D X_S}{2}\right)$$

$$-\ln\left[10\,X_S + \sqrt{\left(\frac{C_D X_S}{2}\right)^2 + 100\,X_S^2}\right]$$

$$-\frac{\rho\,C_D^2\,Q_v\,X_S}{8K}\left[\frac{10\,X_S}{\left(\frac{C_D X_S}{2}\right)^2\sqrt{\left(\frac{C_D X_S}{2}\right)^2 + 100X_S^2}}\right]\frac{\partial X_S}{\partial t}$$

The square root terms in this equation can be approximated using the series expansion.

$$\sqrt{100X_S^2 + \left(\frac{C_D X_S}{2}\right)^2} \doteq 10X_S\left[1 + \frac{C_D^2}{800}\right]$$

The equation for the integral term becomes

$$\frac{\rho}{K}\int_{\textcircled{1}}^{\textcircled{2}}\frac{\partial}{\partial t}\left[\frac{Q_v}{X_S}\right]dy \doteq \frac{\ln(40/C_D)}{2K}\frac{\partial Q}{\partial t} - \frac{\rho Q_v}{2KX_S}\frac{\partial X_S}{\partial t}$$

where $1 + \frac{C_D^2}{800}$ has been approximated by 1. Since C_D is approximately equal to 0.6,

$$\frac{\ln\,(40/C_D)}{2} = 2.0$$

and the final form of the differential equations for the alternating flow through the valve is

$$\frac{dQ}{dt} = \frac{K}{2\rho}\left[P_1 - P_2 + \frac{\rho Q_v}{2KX_S}\,\frac{dX_S}{dt} - \frac{\rho Q_v|Q_v|}{2K^2C_D^2\,X_S^2}\right]$$

When the dynamic terms, $\frac{dQ}{dt}$ and $\frac{dX_S}{dt}$ are negligible this reduces to the form of Bernoulli's equation shown at the beginning of this section.

3.2 SUPERIMPOSED ALTERNATING AND STEADY FLOW

In a transducer utilizing direct modulation of sea water flow to produce an acoustic signal in the water, the pressures and flows have both steady and alternating components. When these pressures and flows encounter an orifice, the amount of pressure drop, power loss, and harmonic content all depend on the relative magnitude of the steady and alternating components.

3.2.1 Pressure Drop and Power Loss in an Orifice When $Q=Q_0+Q_1 \sin (wt) + Q_2 \sin (2\,wt)$

Returning to the basic Bernoulli equation for the flow through an orifice, one can find the pressure drop, P, and instanteneous power loss, W, using the following equations;

$$P = \frac{\rho Q\,|\,Q|}{2\,C_D^2\;A^2}$$

$$W = \frac{\rho Q^2\,|Q|}{2\,C_D^2\,A^2}$$

Where ρ is the fluid density, Q is the instantaneous flow through the orifice, C_D is the discharge coefficient ($C_D \doteq .6$), and A is the orifice area.

In many cases of hydroacoustic devices, there are fixed orifice like constrictions which must pass both steady and alternating flow. Examples are feed tubes and inertance tubes. In such cases the alternating flow causes an increase in the average pressure drop over that which would occur in the case of steady flow only. Also, in such cases the total power loss is of interest in computing overall efficiency and power balance. The following develop expressions for both these quantities. Let the flow be given by

$$Q = Q_0 + Q_1 \sin (wt) + Q_2 \sin (2\ wt).$$

If the instantaneous pressure and power loss are integrated over one cycle, the average pressure and power loss are given by

$$P_{AVE} = K \frac{Q_0^2}{2\ C_D^2 A^2} = K\ P_{ST}$$

$$W_{AVE} = M \frac{Q_0^3}{2\ C_D^2 A^2} = M\ W_{ST}$$

where K and M are functions of Q_1 and Q_2 and P_{ST} and W_{ST} are the pressure drop and power loss respectively in the absence of alternating flow.

If $k_1 = Q_1/Q_0$ and

$$k_2^n = Q_2/Q_1$$

then K and M can be found from Figures 3.2 and 3.3.

If k_2^n is equal to zero and k_1 is large ($k_1 > 5$), then K and M can be approximated by

$$K \approx (1 + 8\,k_1)/2\pi$$

$$M \approx (1 + 12\,k_1 + 8\,k_1{}^3/_3)/2\pi.$$

If k_1 is very large, these expressions become

$$K \approx 4\,k_1/\pi$$

$$M \approx 4k^3/\pi$$

3.2.2 Harmonics of Pressure with $Q = Q_0 + Q_1 \sin(wt)$

In the above section the pressure factor K is calculated to determine the average pressure difference for combined steady and alternating flow through an orifice like constriction when the average pressure difference for steady flow alone is known. In this section an estimate of the magnitude and phase of the higher harmonics is derived for a known flow

$$Q = Q_0 + Q_1 \sin wt.$$

The flow is a result of a pressure difference

$P_0 = C_1\, Q|Q|$ where

$$C_1 = \frac{\rho}{2\,C_D^2\,A^2}$$ and

C_D is the discharge coefficient

A is the area of the orifice.

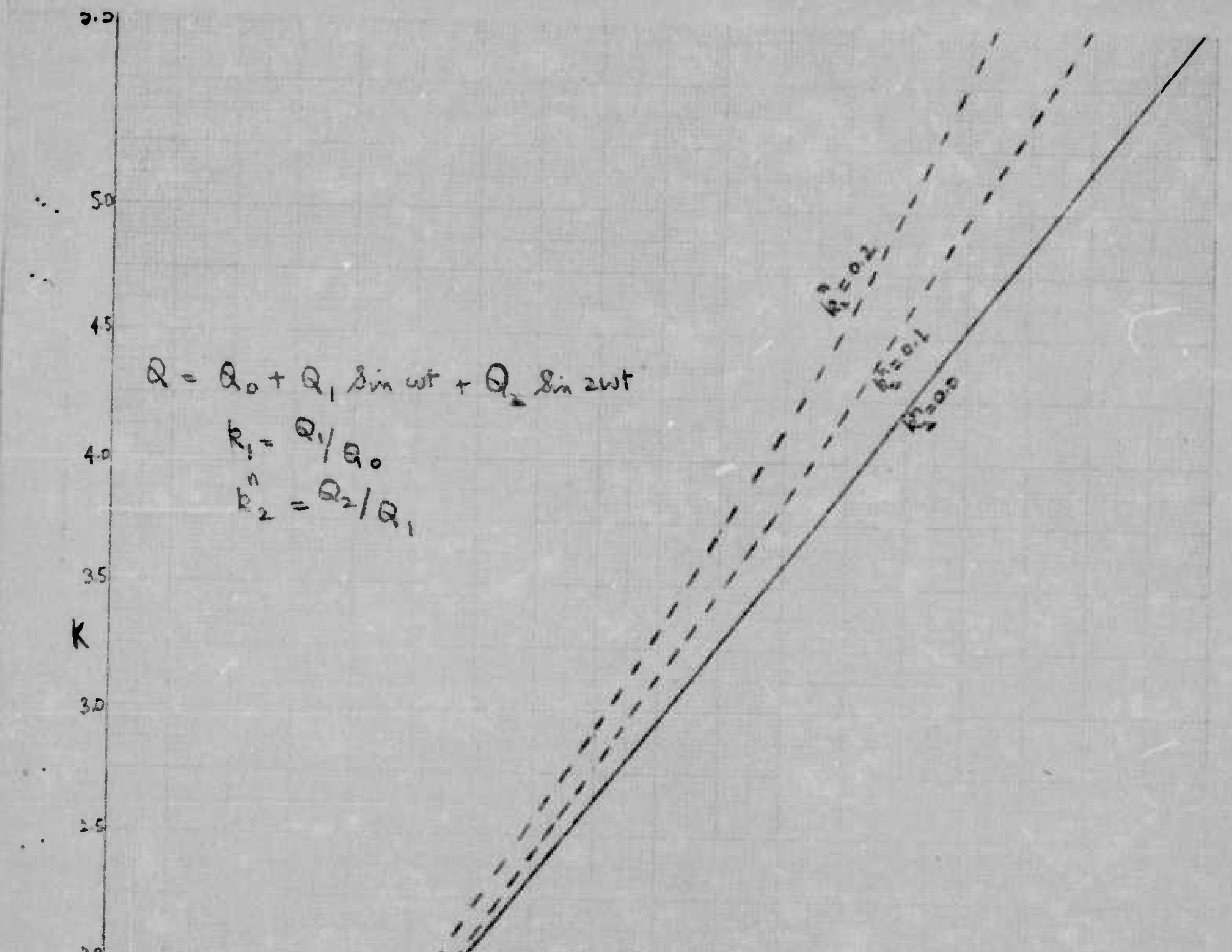

Figure 3.2 Pressure Factor, K, for Superimposed Alternating and Steady Flow.

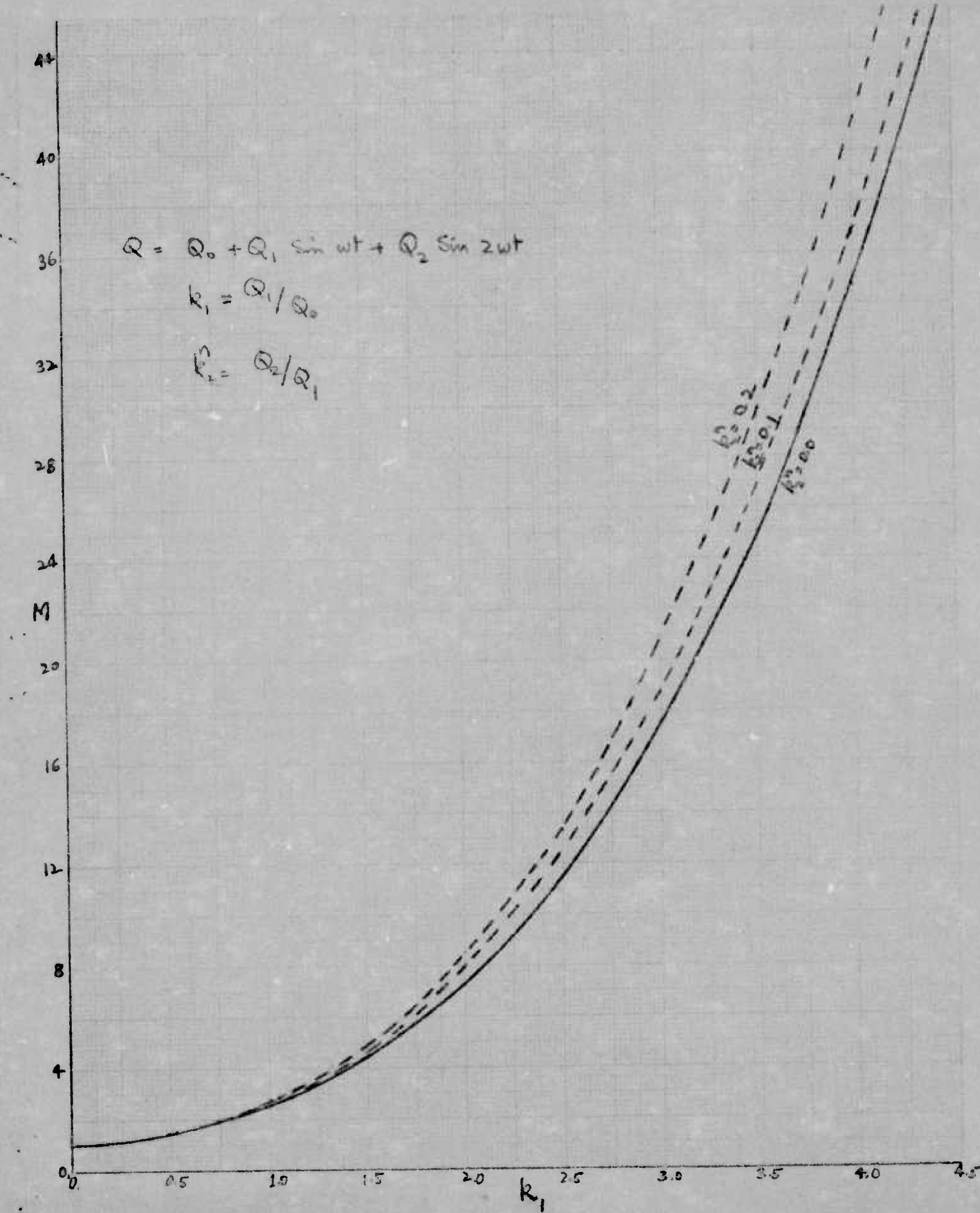

Figure 3.3 Power Factor, M, for Superimposed Alternating and Steady Flow.

Assuming that quasi-static conditions exist for the flow field, the harmonic analysis of P_0 is described as follows. Let

$$P = \frac{P_0}{C_1 Q_0^2} = \sum_{n=0}^{\infty} A_n \sin (N\omega t + \psi_N)$$

where A_n is the magnitude and ψ_n is the phase of the n^{th} harmonic of the normalized pressure. The pressure has been normalized with respect to the pressure in the absence of the alternating flow.

It can be shown that for $n>2$ and $k_1 > 1$ $(k_1 = Q_1/Q_0)$

if n is even

$$A_n = \frac{4}{\pi}\left[\left(1+\frac{k_1^2}{2}\right)\frac{\sin n\phi_1}{n} - k_1\left[\frac{\cos(n-1)\phi_1}{n-1} - \frac{\cos(n+1)\phi_1}{n+1}\right] - \frac{k_1^2}{4}\left[\frac{\sin(n-2)\phi_1}{n-2} + \frac{\sin(n+2)\phi_1}{n+2}\right]\right]$$

if n is odd

$$A_n = \frac{4}{\pi}\left[\left(1+\frac{k_1^2}{2}\right)\frac{\cos n\phi_1}{n} + k_1\left[\frac{\sin(n-1)\phi_1}{n-1} - \frac{\sin(n+1)\phi_1}{n+1}\right] - \frac{k_1^2}{4}\left[\frac{\cos(n+2)\phi_1}{n+2} + \frac{\cos(n-2)\phi_1}{n-2}\right]\right]$$

$$A_1 = 2k_1 + \frac{4}{\pi}\left[(2+k_1^2)\frac{2\cos \phi_1}{3} - \frac{k_1}{2}\left(\pi - 2\phi_1 + \frac{\sin 2\phi_1}{n+2}\right)\right]$$

$$A_2 = \frac{-k_1^2}{4} + \frac{4}{\pi}\left[\frac{(1+k_1^2)}{2}\sin\frac{2\phi_1}{2} - k_1\left(\cos\phi_1 - \cos\frac{3\phi_1}{3}\right)\right.$$

$$\left. + \frac{k_1^2}{4}\left(\pi_2 - \phi_1 - \frac{\sin 4\phi_1}{4}\right)\right]$$

where $\phi_1 = \sin^{-1}\left(\frac{1}{k_1}\right)$ and $\Psi_n = 0$ if N is Odd, or

$\Psi_n = \frac{\pi}{2}$ if n is even.

If $k_1 \leq 1$,

$A_1 = 2\ k_1$

$A_2 = \frac{-k_1^2}{4}$

$A_n = 0$ for $n > 2$

For very large values of k_1,

$A_n = \frac{8\ k_1^2}{\pi n(n^2-4)}$ if n is odd and

$A_n = 0$ if n is even.

These last expressions are the Fourier series for $k_1^2 \sin wt|\sin|wt$ and represent the limit when the steady flow is zero.

Figure 3.4 is a plot of A_n as a function of k_1 for n = 1 to 4. As can be seen from the graph, the first harmonic is predominant and the higher

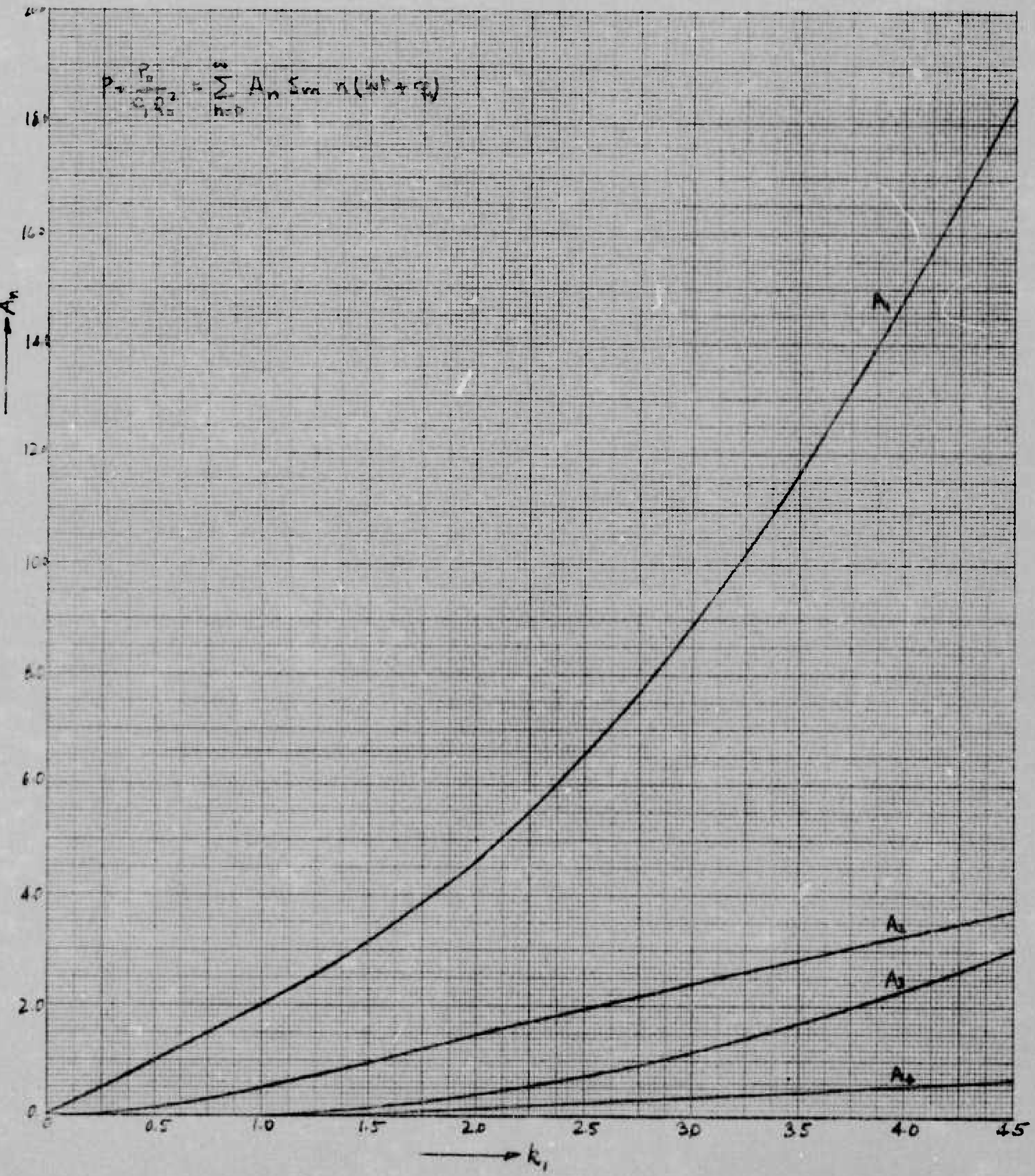

Figure 3.4 First Four Harmonics in the Pressure Across an Orifice when the flow is $Q_0(1 - k_1 \sin wt)$.

harmonics keep on becoming less significant successively. From the above equations, in the limit of large k_1, the magnitudes of the third and fifth harmonic are respectively only about 20% and 3% of the magnitude of the first harmonic while the second and fourth harmonics tend to dissipate altogether.

3.2.3 Harmonic Content of Flow Through a Fixed Orifice when $P = \overline{P} + \hat{P} \sin wt$

Since a fixed orifice is a nonlinear element, it generates harmonics in the flow through it when alternating pressures are applied across it. When the amplitude of the oscillatory pressure is large, the nonlinearities may be significant and the higher harmonics may not be negligible when compared to the fundamental. It is useful to know the relative magnitudes of the harmonics generated by this type of orifice.

Let the pressure upstream of the orifice be

$$P_1 = \overline{P}_1 + \hat{P}_1 \sin wt$$

and the pressure downstream be a constant P_2

If quasi-steady state conditions are assumed to exist, the resulting flow is given by Bernoulli's equation.

$$Q = C\left[\left|F(t)\right|\right]^{\frac{1}{2}} \operatorname{Sgn} F(t)$$

Where $F(t) = \left[(\overline{P}_1 - P_2) + \hat{P}_1 \sin \omega t\right]$

Then $Q = C\left|\bar{P}_1 - P_2\right|^{\frac{1}{2}} \left|1+\alpha \sin wt\right|^{\frac{1}{2}} \operatorname{Sgn}(1+\alpha \sin \omega t) \operatorname{Sgn}(\bar{P}_1 - P_2)$

Where $\alpha = \hat{P}_1/(\bar{P}_1 + P_2)$ or

$$Q^n = \frac{Q}{C\left|\bar{P}_1 - P_2\right|^{\frac{1}{2}} \operatorname{Sgn}(\bar{P}_1 - P_2)} = \left|1+\alpha \sin \omega t\right|^{\frac{1}{2}} \operatorname{Sgn}(1+\alpha \sin \omega t)$$

Where Q^n is the flow normalized with respect to the flow caused by steady pressure difference alone.

A computer program was developed to perform a Fourier analysis on the expression for Q^n and determine the magnitude and phase of the first nine harmonics.

Let $Q_n = \sum_{k=0}^{\infty} C_k \cos(kwt + \Psi_k)$

where C_k is the magnitude of the kth harmonic and Ψ_k is its phase angle.

$$Q_n = C_1 \sum_{0}^{\infty} \left[C_k/C_1 \cos(kwt + \Psi_k)\right] \text{ or}$$

$$Q_n = C_1 \sum_{0}^{\infty} C_k^n \cos(kwt + \Psi_k)$$

where C_k^n is magnitude of the kth harmonic normalized with respect to that of the first harmonic.

Figure 3.5 shows the magnitude and phase angle of the first four terms in this expression for various values of the modulation factor α. For the range of α covered here, the second harmonic is always in phase with the fundamental and reaches a peak of .32 at a modulation factor of 1.2. The third harmonic is less than .15 and is in phase with the fundamental up to a modulation factor of approximately 2.0 at which point it becomes out of phase with the fundamental. As α is reduced to zero, all the harmonics approach zero and the flow is given by the steady flow component. It can also be seen from the figure that as α increases, the second harmonic tends to decrease slowly while the third harmonic does not follow this pattern. In the limit of α very large, $(1 + \alpha|\text{Sin } wt|)^{\frac{1}{2}} \approx \alpha^{\frac{1}{2}} |\text{Sin } wt|^{\frac{1}{2}}$ and the magnitude of the Fourier components of $\text{Sin}|wt|^{\frac{1}{2}}$ is given by

$$C_k = \frac{8(2\pi)^{\frac{1}{2}}}{1-4k^2} \left[\Gamma\frac{(1+2k)}{4}\,\Gamma\frac{1-2k}{4}\right]^{-1} \quad \text{if n is odd}$$

$$C_k = 0 \text{ if n is even}$$

where Γ is the gamma function.

Thus for very large α only the odd harmonics are present while the even harmonics become insignificant.

3.2.4 Harmonics of the Flow Through a Varying Orifice with Sinusoidal Pressure Difference.

Another case of interest is that of an orifice whose opening varies sinusoidally over one-half cycle and is zero for the other half cycle.

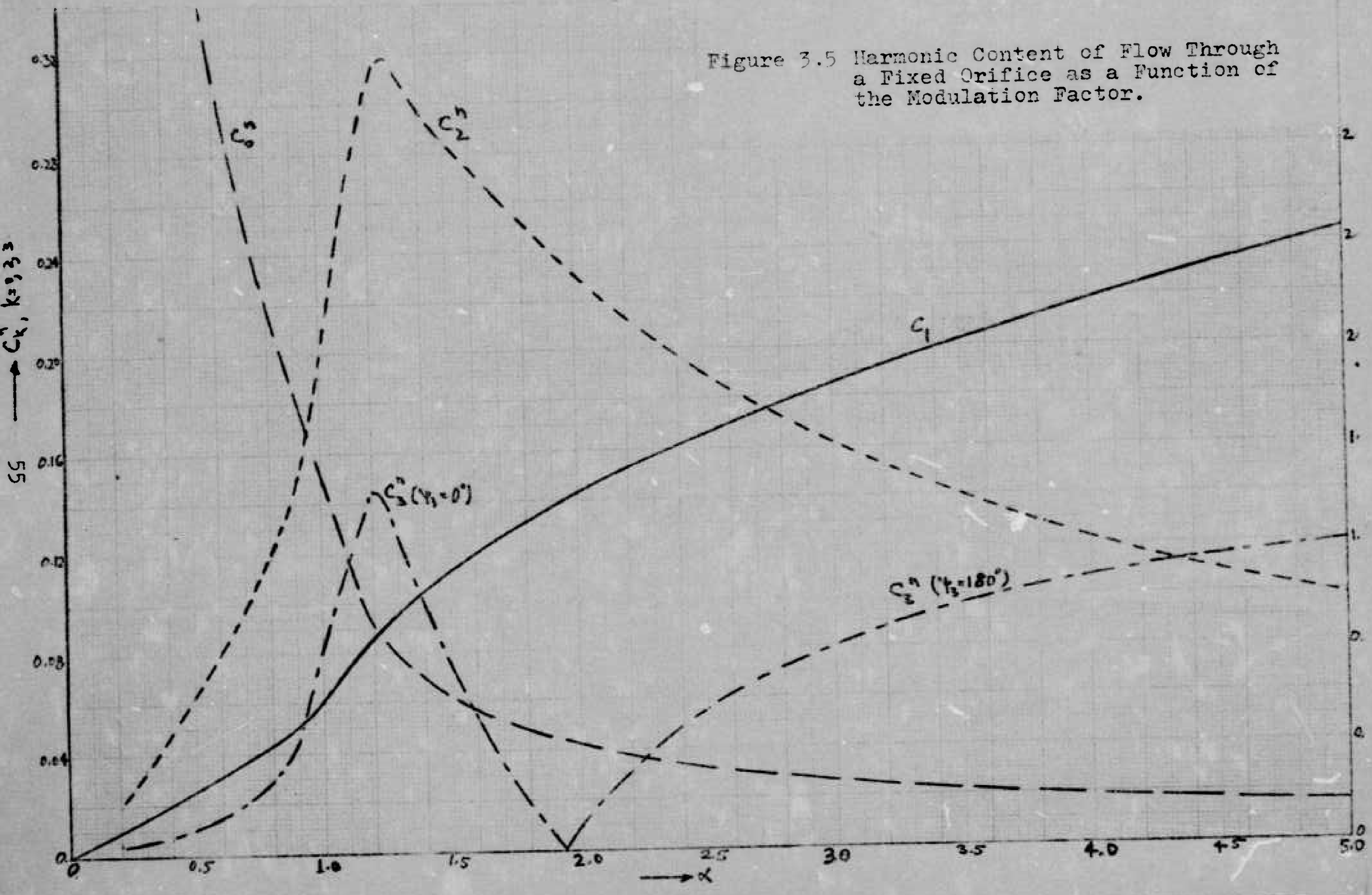

Figure 3.5 Harmonic Content of Flow Through a Fixed Orifice as a Function of the Modulation Factor.

If the pressure difference between the two sides of the orifice is sinusoidal or predominantly sinusoidal and the pressure is in phase with the opening, a closed form solution for the harmonic analysis can be obtained as follows:

$$\text{Let } P = \hat{P} \sin wt$$

$$\text{and } X = \hat{X} \sin wt \quad \text{if } \sin wt > 0$$

$$X = 0 \qquad \text{if } \sin wt \leq 0$$

Where X is the linear orifice opening the flow $Q = C_D A \mathcal{v}$ or

$$Q = C_D WX \sin wt \, (P \sin wt)^{\frac{1}{2}}$$

Where W is the width of the orifice opening and $Cq = \sqrt{\frac{2g}{\rho}} \, C_D$.

$$Q^n = \frac{Q}{C_q W\hat{X} \, \hat{P}^{\frac{1}{2}}} = (\sin wt)^{3/2} \text{ if } \sin wt > 0$$

$$= 0 \quad \text{if } \sin wt \leq 0$$

The Fourier series representation of Q^n is

$$Q^n = \frac{1}{\pi}\left[\frac{A_o}{2} + \sum_{n=1}^{\infty} (A_n \cos nwt + B_n \sin nwt)\right]$$

where $A_n = 0$ if n is odd, and

$$A_n = \frac{\pi(-1)^{n/2}}{5\sqrt{2}\,\beta\left(\frac{n}{2} + \frac{7}{4}, \frac{7}{4} - \frac{n}{4}\right)} \text{ if n is even,}$$

and $B_n = 0$ if n is even, and

$$B_n = \frac{\pi(-1)^{\frac{(n+1)}{2}}}{5\sqrt{2}\,\beta\left(\frac{n}{2} + \frac{7}{4}, \frac{7}{4} - \frac{n}{2}\right)}$$

where β is the Beta function

$$\beta\left(\frac{7}{4} + \frac{n}{2}, \frac{7}{4} - \frac{n}{2}\right) = \frac{\Gamma(7/4 + \frac{n}{2})\Gamma(\frac{7}{4} - \frac{n}{2})}{\Gamma(7/2)}$$

$$Q = \frac{.874}{\pi} + \frac{1.44}{\pi}\left[\cos wt - .528 \sin 2\,wt - .111 \cos 3\,wt - .047 \sin 4\,wt - .026 \cos 5\,wt\right]$$

The above analysis indicates that second harmonic is significant (more than 50% of the first) while higher harmonics are substantially less in magnitude.

3.3 PARAMETRIC PERFORMANCE, HARMONIC ANALYSIS AND TRADE-OFF DATA FOR HYDROACOUSTIC POWER OSCILLATORS

One form of the hydroacoustic power oscillator is shown in Figure 3.6 which utilizes a variable orifice valve to modulate the flow of sea water from the sea pressure head to an evacuated reservoir. The spool valve is driven with a nearly sinusoidal force by the oscillator sections at either end of the spool.

The basic differential equations for the power oscillators have been programmed into a previously developed computer program which solves sets of coupled, first-order, ordinary, differential equations. This model is then used to simulate the harmonic content of the pressure applied to the acoustic transmission line and thence into the water. It is

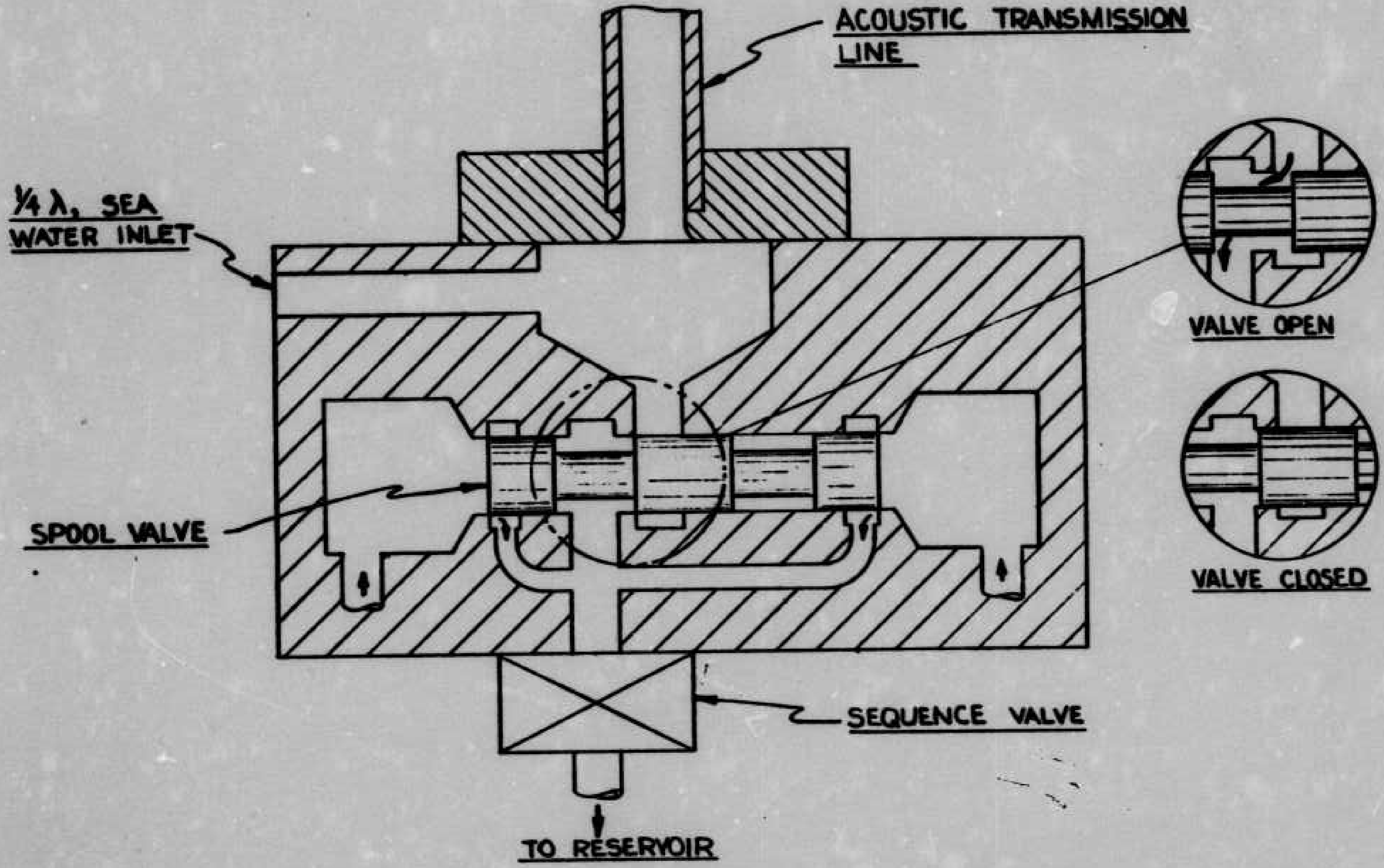

Figure 3.6 Basic Hydroacoustic Power Oscillator which Modulates the Flow of Sea Water.

also used to generate parametric data relating input and output power, efficiency, average flow, peak valve spool displacement and diameter, and pressure modulation coefficient to the acoustic load impedance, (both magnitude and angle), fundamental frequency of oscillation, and pressure head. This data is used to select the optimum hydroacoustic power oscillator parameters for a wide range of applications. The results have been normalized with respect to the acoustic load impedance, operating frequency, and acoustic filter parameters. Table 3-1 presents the glossary of symbols and normalizing factors used in this section.

3.3.1 Basic Power Oscillator Circuits

Two basic types of hydroacoustic power oscillators are considered in this report. The first (shown in Figure 3.7a) is similar to the device shown in Figure 3.6 and is designated as a single-ended oscillator. The second (shown in Figure 3.8a) is designated as a double-ended oscillator. It will be shown in this section that the performance of the double-ended oscillator can be directly related to the performance of the single-ended oscillator.

Figure 3.7b shows an equivalent representation of the single-ended oscillator section of the hydroacoustic transducer shown in Figure 3.6. The single orifice is fed by sea water pressure, P_S, through a long tube of equivalent inertance L and a cavity of compliance C. The flow through the oscillator is modulated by a valve spool whose displacement is given by X_T sin wt. A typical flow waveform for this class of oscillator is shown in Figure 3.7c.

TABLE 3.1 SYMBOLS USED IN SECTION 3.3

Hydraulic Pressures (psi)

P_S	Supply Pressure
P_V	Average pressure difference across the orifice $P_V = P_S$ for a single-ended oscillator $P_V = P_S/2$ for a double-ended oscillator
$P_L(t)$	The pressure across the load P_L = amplitude of the fundamental of $P_L(t)$ $\bar{P}_L$ = average pressure across the load $\bar{P}_L = P_S$ for a single-ended oscillator $\bar{P}_L = P_S/2$ for a double-ended oscillator

Hydraulic Flows (cis)

$Q_S(t)$	Flow through feed inertance L from supply pressure to the valve $\bar{Q}_S$ = average flow from the supply pressure source
$Q_V(t)$	Flow through the orifice or valve $\bar{Q}_V$ = average valve flow (equal to $\bar{Q}_S$)
$Q_L(t)$	Flow through the load $Q_L(t) = P_L(t)/R_L$ $\bar{Q}_L$ = average flow through load ($\bar{Q}_L = 0$) Q_L = amplitude of the fundamental of $Q_L(t)$
H_k	Amplitude of k^{th} harmonic of a flow

Valve Parameters

D_V	Metering diameter of the valve

TABLE 3.1 (continued)

P_F	Porting fraction
K	Porting length ($K = \pi D_V P_F$)
$X_S(t)$	Valve displacement $X_S(t) = X_T \sin wt$ X_T = amplitude of valve displacement w = angular driving frequency f = driving frequency ($f = 2\pi\omega$)
C_q	Discharge coefficient of valve (C_q = 92 for sea water) $C_q = C_D\sqrt{2/\rho}$ C_D = contraction coefficient ρ = density of fluid
L_V	Total flow inertance in series with valve. $L_V = 2\rho/K + L_{US} + L_{DS}$ L_{US} = Upstream flow inertance L_{DS} = Downstream flow inertance

Load Parameters

R_L	Load resistance
L	Inlet path flow inertance ($L = \rho\ell/A$) ρ = fluid density ℓ = length of flow path A = cross-section area of flow path

TABLE 3.1 (continued)

C	Load cavity compliance ($C = V/\rho c^2$) V = load cavity volume ρ = fluid density c = speed of sound in fluid
Q	Load Q factor (parallel R-L-C circuit) $Q = \omega_o C R_L = R_L/\omega_o L$
ϕ	Phase angle of load on valve
f_o	Tuned frequency of load circuit $f_o = 2\pi\omega_o$ $\omega_o = 1/(LC)^{\frac{1}{2}}$
Performance	Parameters
W_i	Input power ($W_i = P_S\bar{Q}_V/8.86$ Watts)
W_o	Output power ($W_o = P_L Q_L/17.72$ Watts)
η	Efficiency ($\eta = W_o/W_i$)
F_Q	Normalizing factor for flows $F_Q = C_q \pi D_V X_T \sqrt{P_V}$
F_W	Normalizing factor for power $F_W = C_q \pi D_V X_T P_S \sqrt{P_V}$
F_{RL}	Normalizing factor for load resistance $F_{RL} = \sqrt{P_V} / (C_q \pi D_V X_T)$

TABLE 3.1 (continued)

Normalized Variables

K_ω	Normalized frequency $K_\omega = w/w_o = f/f_o$
K_{RL}	Normalized load resistance $K_{RL} = R_L/F_{RL}$
W_{in}	Normalized input power $W_{in} = W_i/F_W$
$\bar{Q}_{Vn}$	Normalized average flow through valve $\bar{Q}_{Vn} = \bar{Q}_V/F_Q$
α	Modulation Coefficient ($\alpha = P_L/\bar{P}_L$) $\alpha = \hat{P}_L/P_S$ for single-ended oscillator $\alpha = 2\hat{P}_L/P_S$ for double-ended oscillator
HDI	Harmonic distortion index $\mathrm{HDI} = \left(\sum_{k=2}^{9} H_k^2\right) \Big/ \left(\sum_{k=1}^{9} H_k^2\right)$

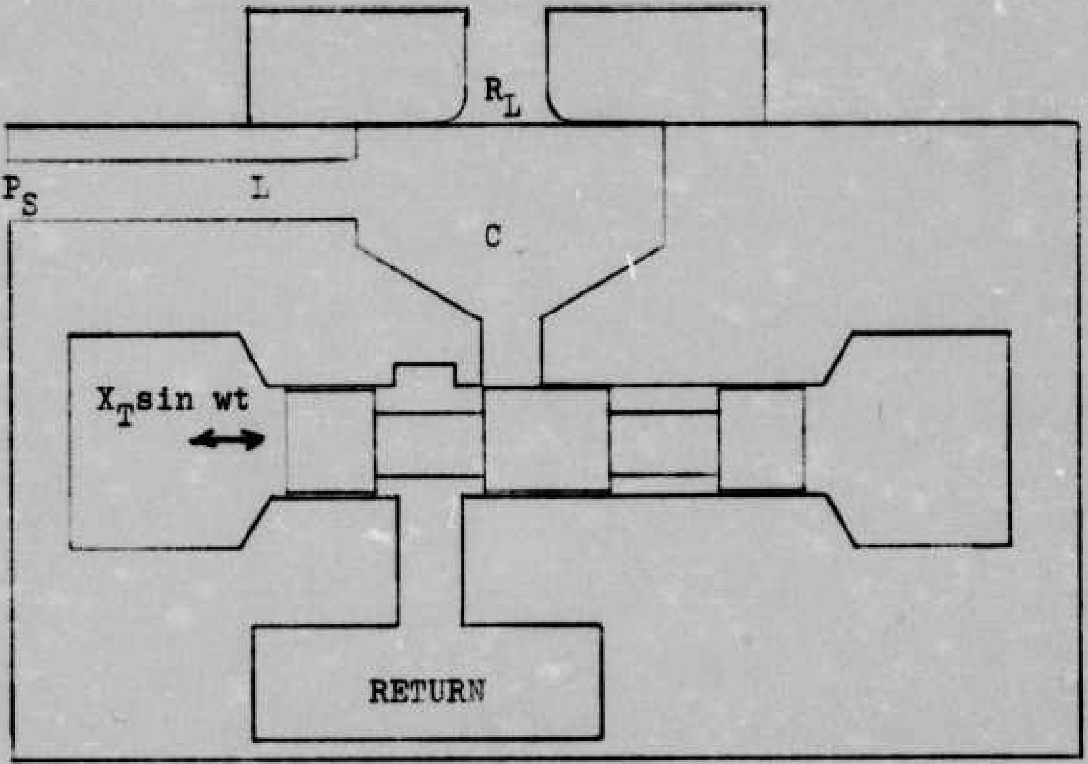

a. Schematic Diagram

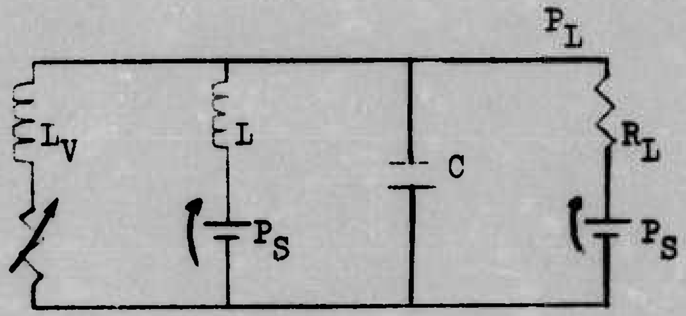

b. Equivalent Representation

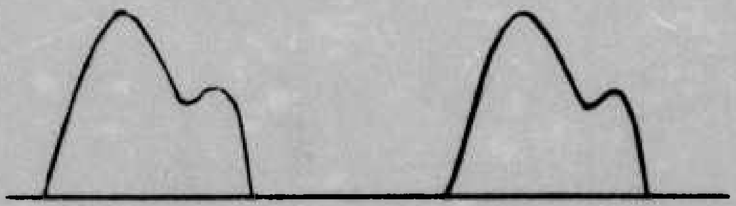

c. Typical Waveform for Flow Through the Valve

Figure 3.7 Basic single Ended Hydroacoustic Power Oscillator

The flow finally goes into a low pressure reservoir (assumed here to have a constant pressure of zero).

Figure 3.8a is a sketch of a symmetrical, double-ended, power oscillator with two variable orifices that alternately modulate the flow into and out of the load cavity. Figure 3.8b is the analogous representation of Figure 3.8a. In this device, the flow is caused by a pressure differential between the supply pressure and the average pressure at load driving one half of the cycle. During the other half, the flow occurs from the load cavity to the return pressure line through another orifice. Since, on a steady basis, there is no flow through the load and the average flow into the load cavity during first half cycle must be equal to average outflow during the other half, the mean differential pressures at load relative to supply pressure and to the return pressure must be equal as seen in Figure 3.8c, the flow waveform for a double-ended oscillator is similar to that for the single-ended case for the first half cycle the flow waveform is repeated, but with the opposite sign.

The performance parameters for the double-ended power oscillator can be directly related to the parameters for the single-ended case. When the two configurations are operated at the same output power level with the same supply pressure, the average differential pressure across the valve for the double-ended case is $P_S/2$ and P_S for the single-ended case. This leads to the following relationships between single and double-ended parameters.

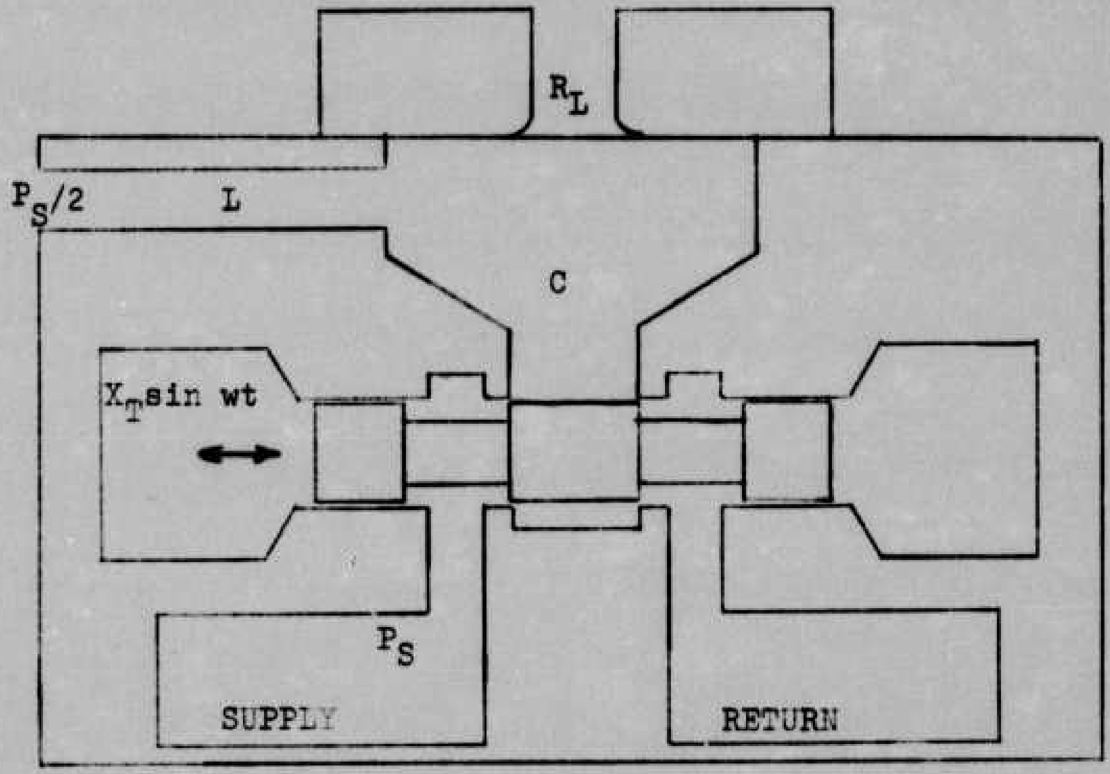

a. Schematic Diagram

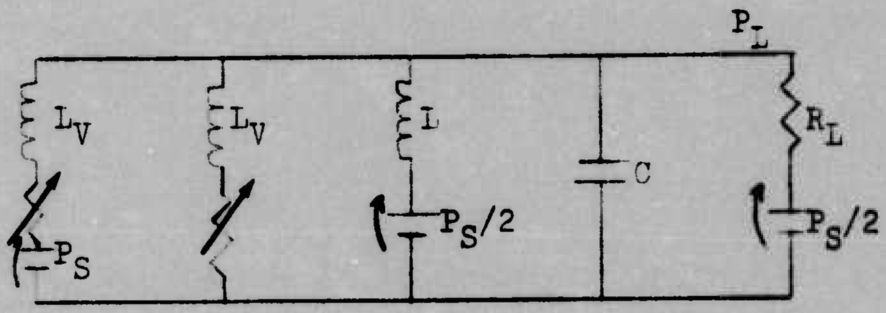

b. Equivalent Representation

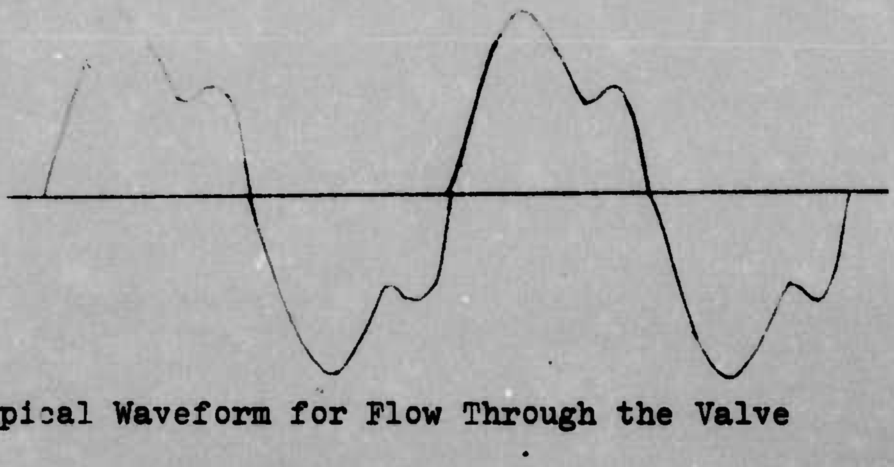

c. Typical Waveform for Flow Through the Valve

Figrue 3.8 Basic Double Ended Hydroacoustic Power Oscillator

$$(D_V\ X_T)_D = \sqrt{2}\ (D_V\ X_T)_S$$

$$(\bar{Q}_V)_D = (\bar{Q}_V)_S$$

$$(\hat{Q}_L)_D = 2\ (\hat{Q}_L)_S$$

$$(W_o)_D = (W_o)_S$$

$$(W_i)_D = (W_i)_S$$

$$(\eta)_D = (\eta)_S$$

$$(\alpha)_D = (\alpha)_S$$

$$(R_L)_D = (R_L)_S/4$$

$$(P_S)_D = (P_S)_S$$

Comparing the Fourier series expansion of $(Q_V(t))_D$ to that of $(Q_V(t))_S$* shows that the even harmonics in the double-ended case are zero, and the odd harmonics (including the first) are twice those of the single-ended case.

$*(Q_V(t))_S = f(wt) \quad wt = 0 \text{ to } \pi$

$\qquad\qquad = 0 \quad wt = \pi \text{ to } 2\pi$

$(Q_V(t))_D = f(wt) \quad wt = 0 \text{ to } \pi$

$\qquad\qquad = -f(wt-\pi) \quad wt = \pi \text{ to } 2\pi$.

3.3.2 Normalizing Factors

The performance of many different power oscillators operating into many different loads can be expressed in several graphs using nondimensional quantities for the output parameters. In this report the output parameters of interest are the average flow through the valve, $\bar{Q}_V$, (which is equal to the average flow from the power source, $\bar{Q}_S$); the input power, W_i; the output power, W_o; the efficiency, η; (η is equal to W_o/W_i); the amplitude of the fundamental harmonic of the pressure at the load, P_L; and the harmonic content of the pressure at the load. The normalizing factors for the first three parameters ($\bar{Q}_V$ W_i, and W_o) are given in Table 3.1 along with the normalizing factors for the load and operating frequency. Efficiency is already normalized so no factor is needed in this case. The first harmonic of load pressure is normalized by dividing it by the average pressure at the load and calling the result the modulation coefficient α.

The harmonic content is normally measured by a factor called Total Harmonic Distortion:

$$\mathrm{THD} = \left[\sum_{k=2}^{\infty} \left(\frac{H_k}{H_1}\right)^2\right]^{1/2}$$

The typical harmonic analyzer which is used to estimate this distortion normally measures another factor defined below.

$$\text{Harmonic distortion} = \left[\frac{\sum\limits_{k=2}^{\infty} H_k^2}{\sum\limits_{k=1} H_k^2}\right]^{1/2}$$

This factor is close to total harmonic distortion if the second and higher harmonics are not large compared to the first harmonic. In this report, the square of the above quantity is used which is called here the harmonic distortion index (HDI) i.e;

$$\mathrm{HDI} = \frac{\sum_{k=2}^{9} H_k^2}{\sum_{k=1}^{9} H_k^2}.$$

The first nine harmonics are included in HDI.

If the driving frequency is different from the resonant frequency of the filter circuit, the load will not be truly resistive but will have a reactive component whose sign depends on the frequency. It can be easily shown that for a parallel R-L-C circuit, the phase angle ϕ is given by

$$\tan\phi = \frac{1 - (f/f_o)^2}{(f/f_o)\, Q}$$

The results from using three phase angles (0°, 45° and 60°) are presented in Section 3.3.4.

3.3.3 Mathematical Model

The behavior of the single-ended hydroacoustic power oscillator shown in Figure 3.7 can be described by the following differential equations.

$$\frac{dQ_V}{dt} = \frac{1}{L_V}\left[P_L + \frac{\rho Q_V}{2KX_S}\frac{dX_S}{dt} - \frac{Q_V\,|Q_V|}{2K^2 C_D^2 X_S^2} \right] \text{For } X_S > 0$$

$$\left.\begin{aligned} \frac{dQ_V}{dt} &= 0 \\ Q_V &= 0 \end{aligned}\right\} \text{ For } X_S \leq 0$$

$$\frac{dQ_S}{dt} = \frac{1}{L}\left[P_S - P_L\right]$$

$$\frac{dP_L}{dt} = \frac{1}{C}\left[Q_S - Q_V - P_L/R_L\right]$$

The variables Q_V, Q_S, and P_L are all zero at time equal to zero. These equations are solved using a previously developed computer program which performs a numerical integration of coupled, non-linear, first order differential equations. The time integration is continued until the transient part of the solution has died out and only the steady-state solution remains.

3.3.4. Presentation of Results

Figures 3.9 a, b, and c are plots of the modulation factor α and the harmonic distortion index HDI as a function of the normalized resistance K_{RL} for different values of Q (1.0, 3.0 and 5.0 respectively). These plots have three curves each for the two variables α and HDI, representing three typical values of phase angle ϕ of the load. The modulation factor α in every case goes up sharply until K_{RL} reaches about 8.0 and then tends to level off. Also there is no remarkable variation in α from one case to another. The magnitude of the first harmonic of the pressure in the load, P_L, is given by αP_S. The presence of higher harmonics is measured by the harmonic distortion

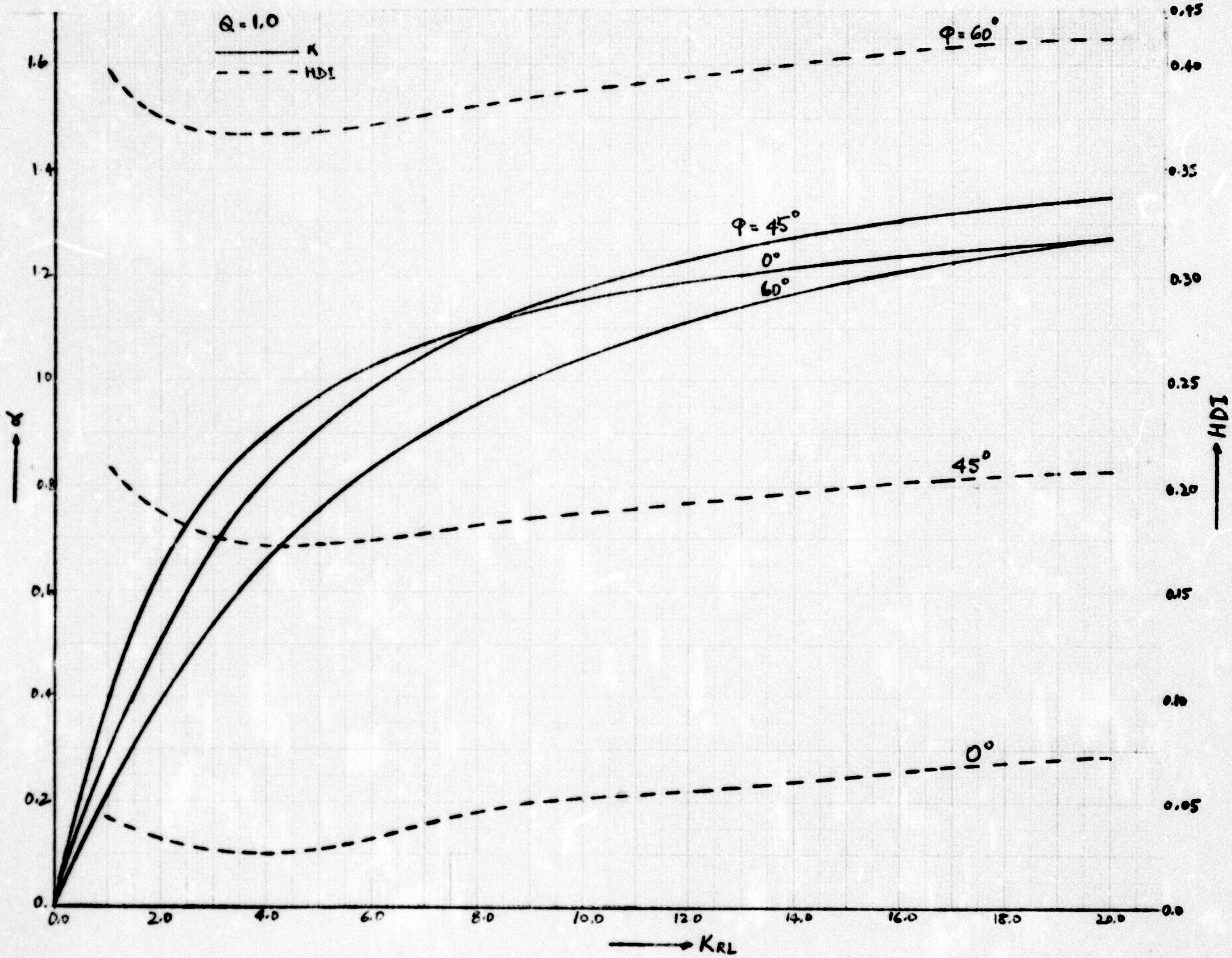

Figure 3.9a Variation of α and HDI as a Function of K_{RL} for Different Values of ∅ . Q = 1.0

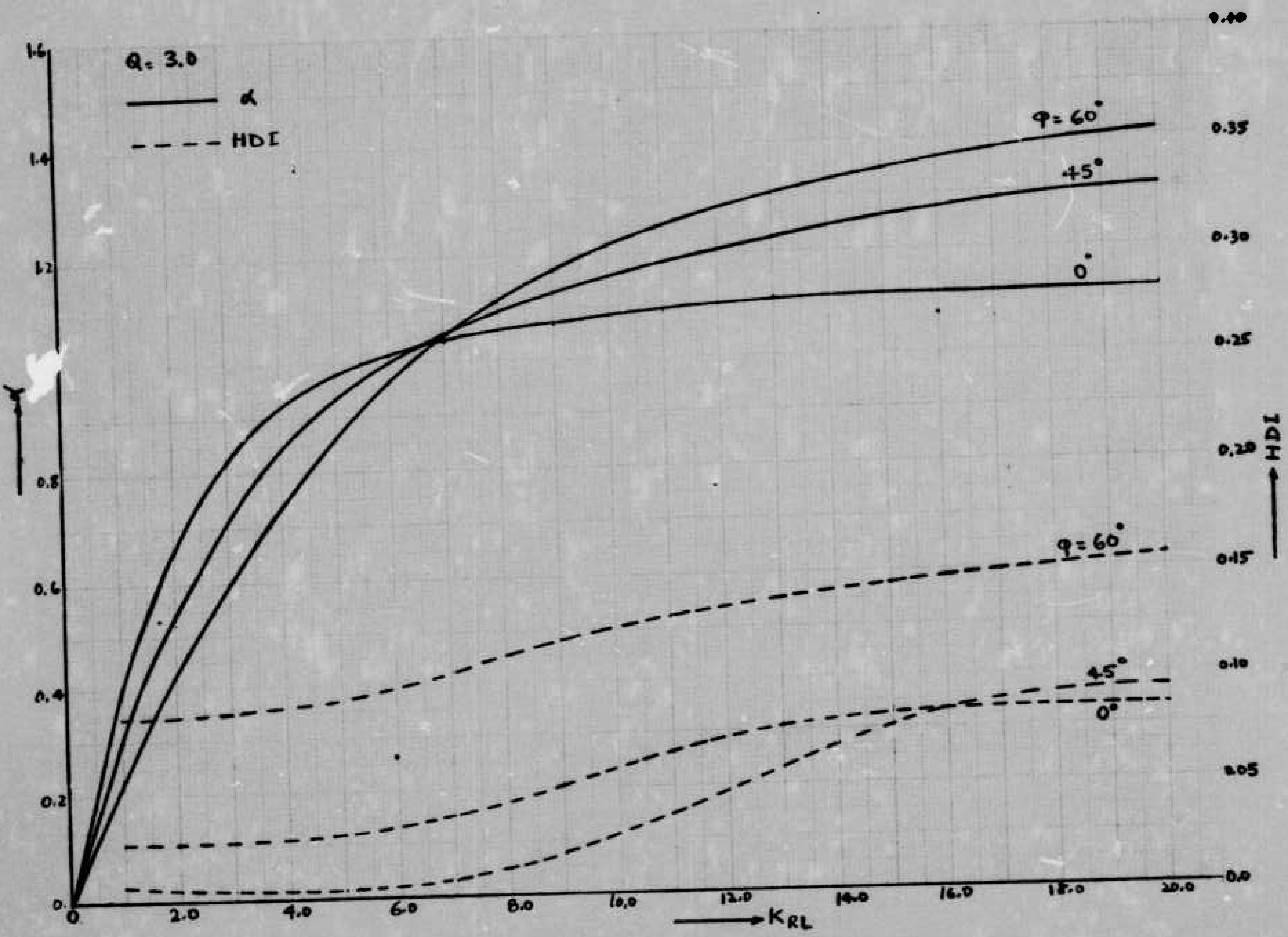

Figure 3.9b Variation of α and HDI as a Function of K_{RL} for Different Values of ϕ . Q = 3.0

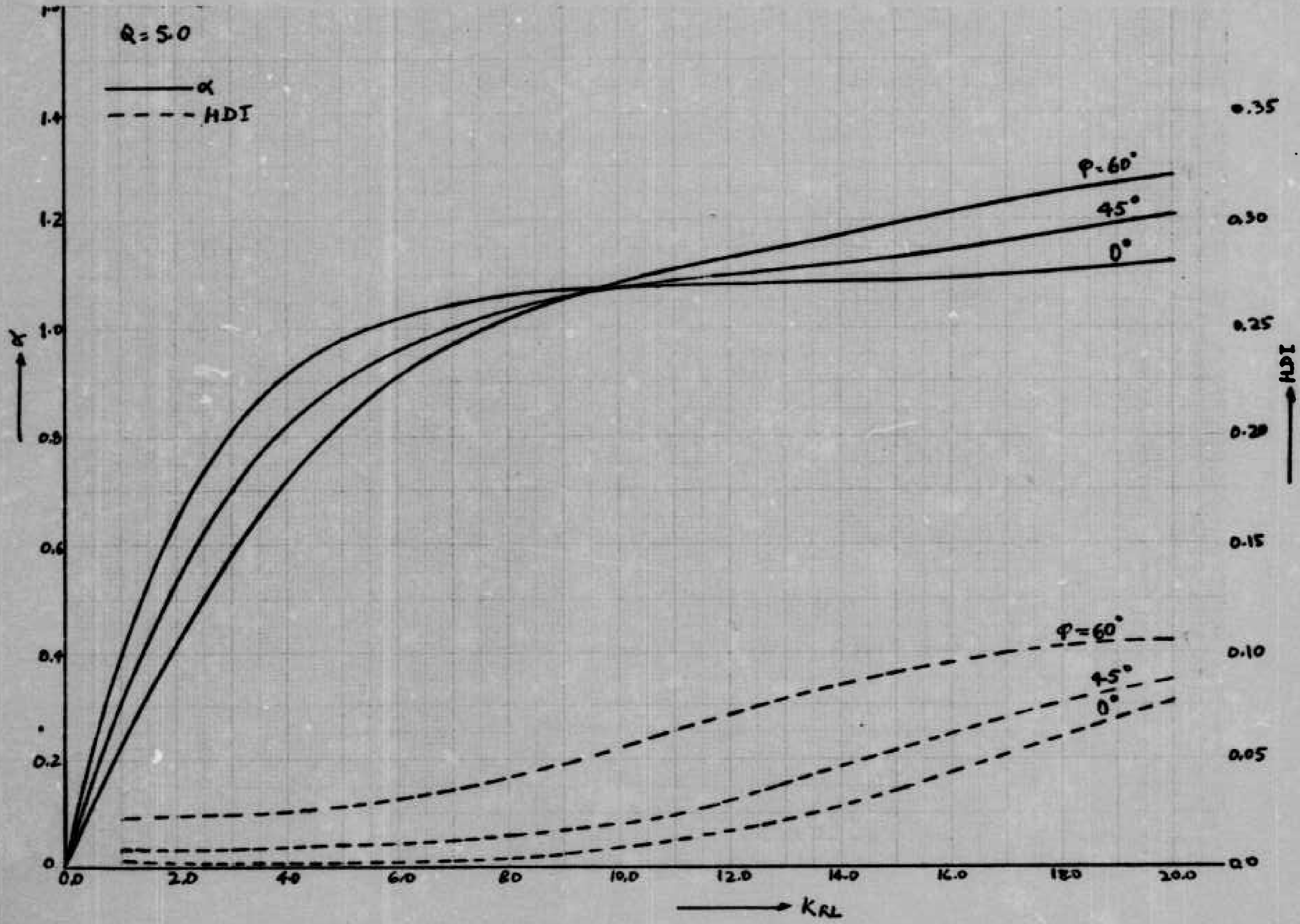

Figure 3.9c Variation of α and HDI as a Function of K_{RL} for Different Values of ϕ. Q = 5.0

index as previously defined. Significant variation in this parameter is expected as Q, a measure of filtering characteristics, is increased. Figure 3.9a indicates that harmonic distortion is greatly increased as the load phase angle increases when the driving frequency shifts away from the resonance frequency of the load circuit. A similar trend also is indicated by Figures 3.9 b and c although the relative magnitude of the difference becomes less predominant as K_{RL} increases. The value of HDI decreases sharply as Q is raised from 1 to 3. A minor reduction results as Q increases from 3 to 5. Also, for every case, the value of HDI goes up slowly up to values of K_{RL} from 6.0 to 8.0, then shows an almost abrupt rise in rate of increase and then tends to level off for values of K_{RL} around 18. There is also a slight reduction (more noticeable when Q is equal to 1) in HDI as K_{RL} varies from 1.0 to 5.0.

Figures 3.10 a, b, and c are plots of efficiency η as a function of normalized resistance K_{RL}. Efficiency, like α, increases rapidly for values of K_{RL} between 0.0 and 6.0. For Q equal to 1.0, the efficiency increases monotonically for increasing K_{RL} and shows a considerable decline as ϕ increases from 0° to 45° and then to 60°. For Q equal to 3.0 or 5.0, the same trend exists for values of K_{RL} the efficiency becomes greater for higher values of ϕ as indicated by Figures 3.10 b and c.

Figures 3.11 a, b, and c form a set of plots of W_{in} and W_{on} as a function of K_{RL} where W_{in} and W_{on} are the normalized input and output power respectively.

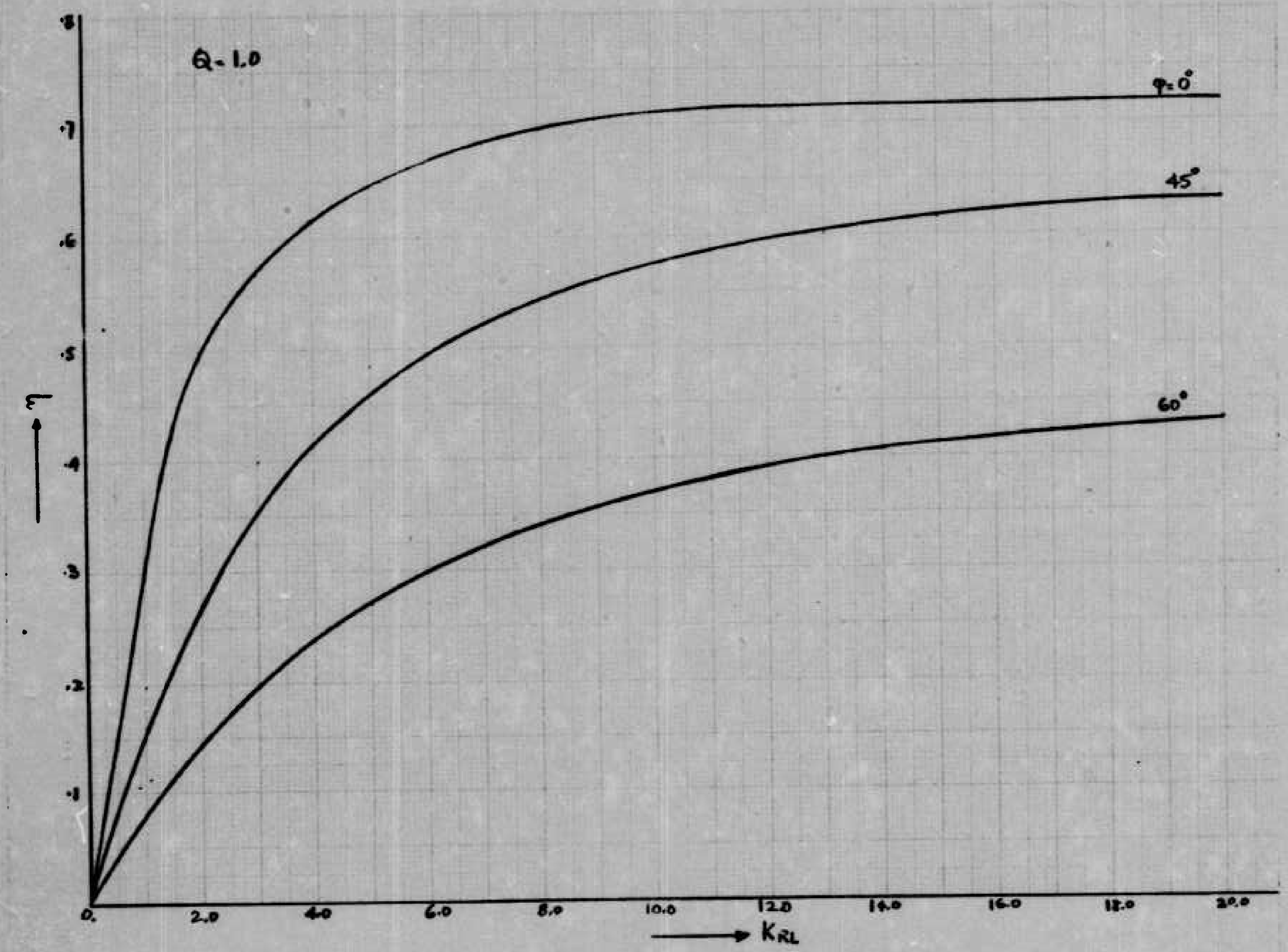

Figure 3.10a Variation of Efficiency η with K_{RL} for Different Values of ϕ.
Q = 1.0

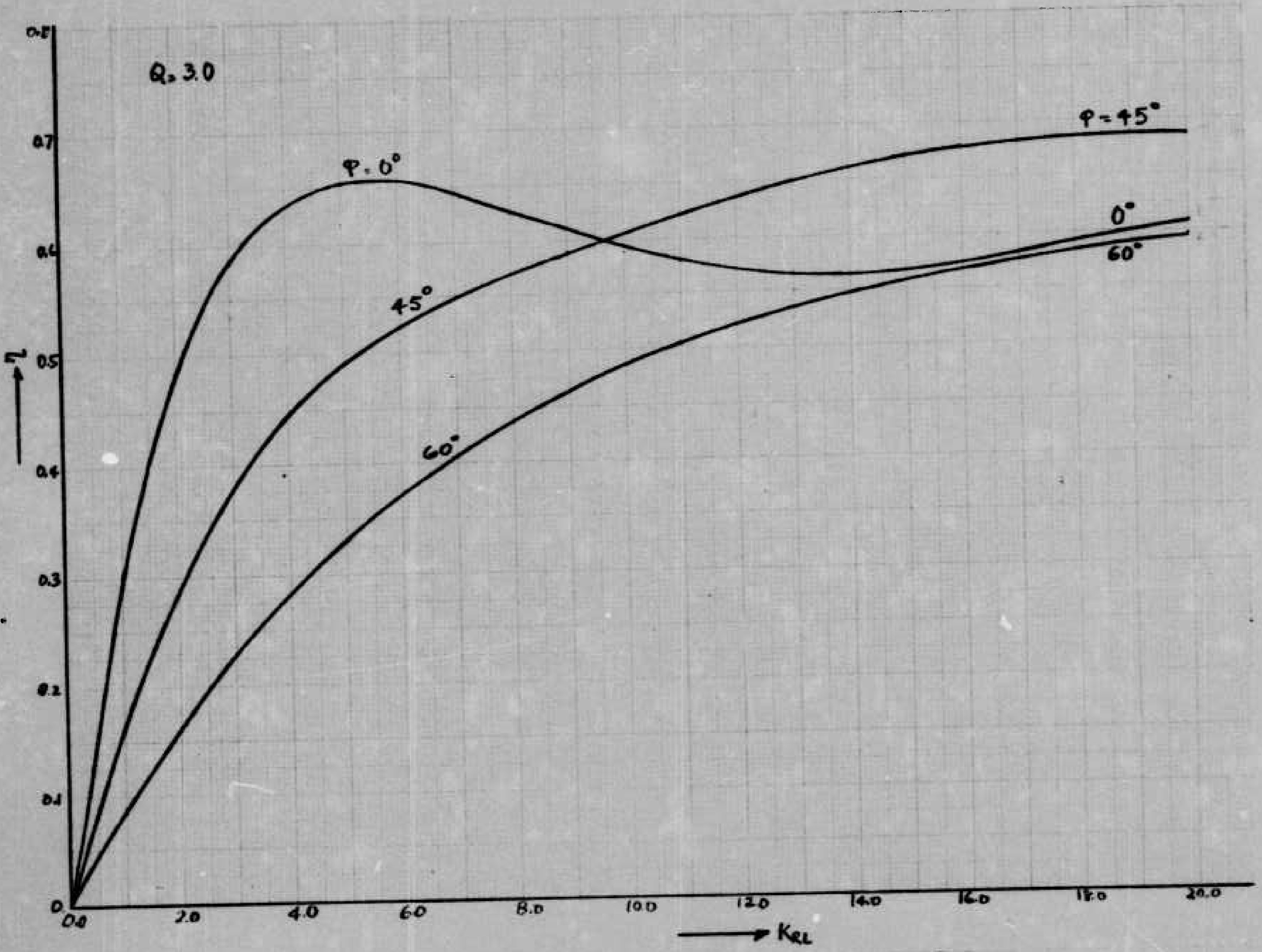

Figure 3.10b Variation of Efficiency η with K_{RL} for Different Values of ϕ . $Q = 3.0$

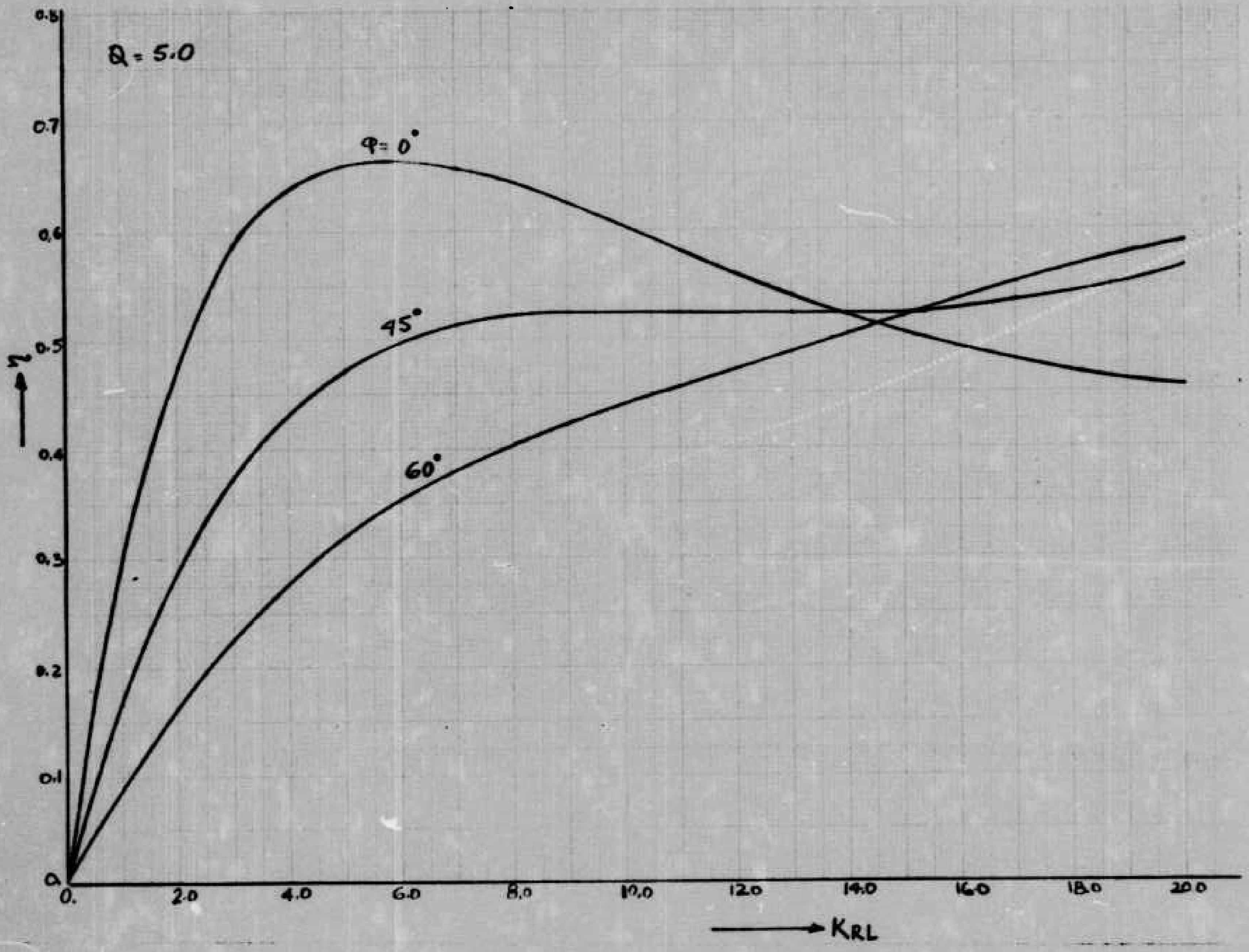

Figure 3.10c Variation of Efficiency η with K_{RL} for Different Values of ϕ.
Q = 5.0

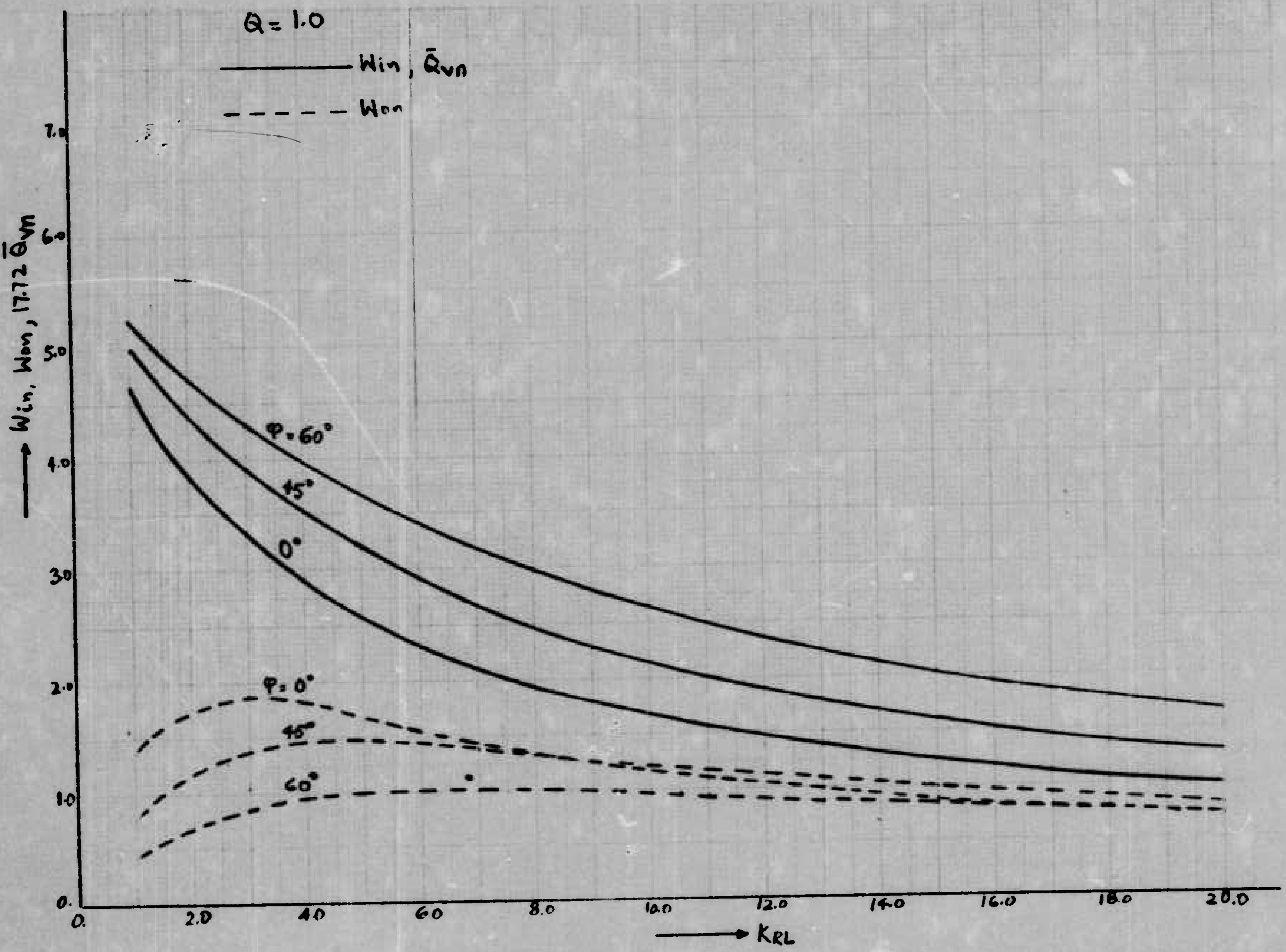

Figure 3.11a Normalized Values of Input Power, Output Power and Average Flow as a Function of K_{RL} for Different Values of Ø. Q = 1.0

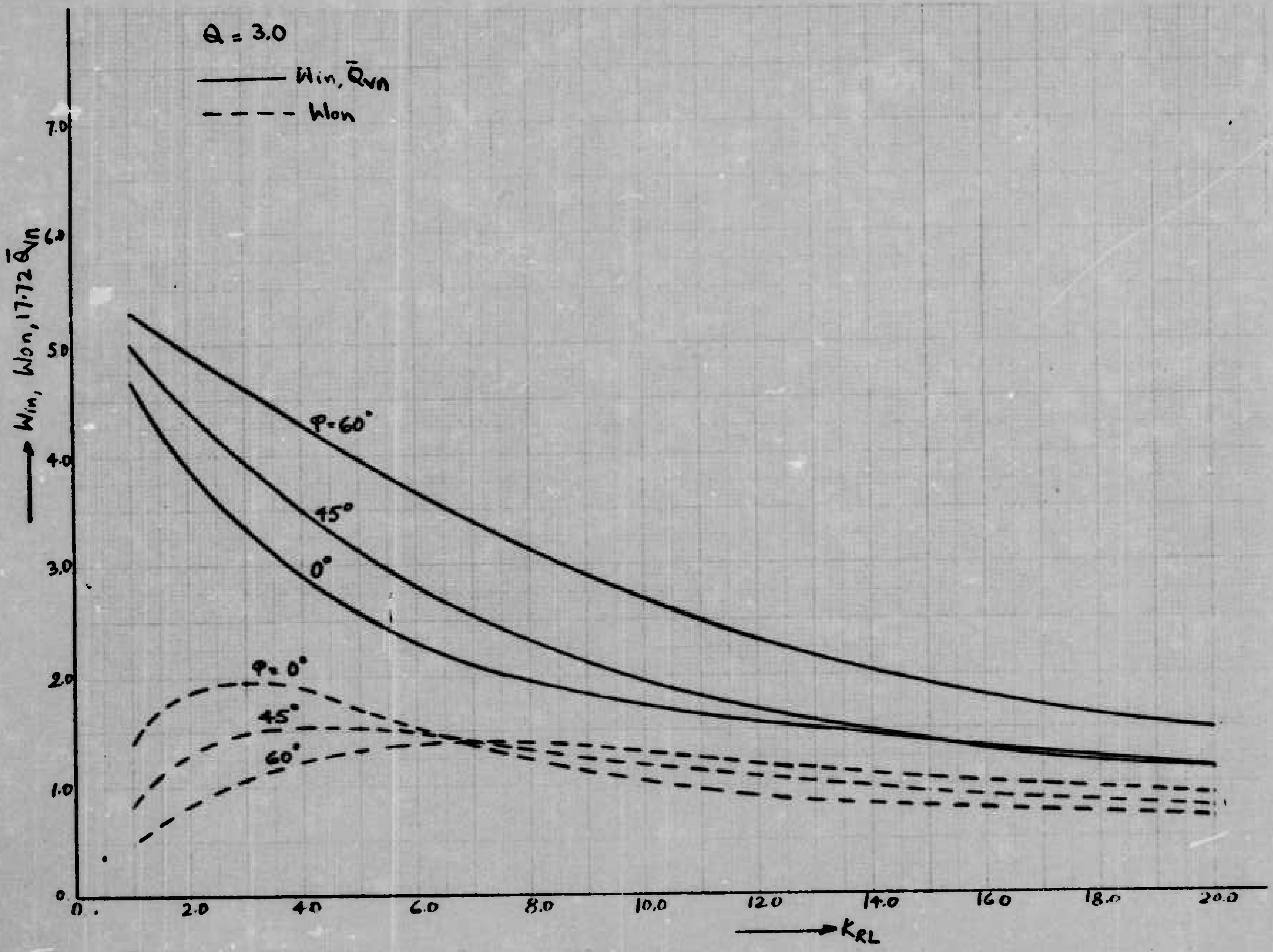

Figure 3.11b Normalized Values of Input Power, Output Power and Average Flow as a Function of K_{RL} for Different Values of Ø. Q = 3.0

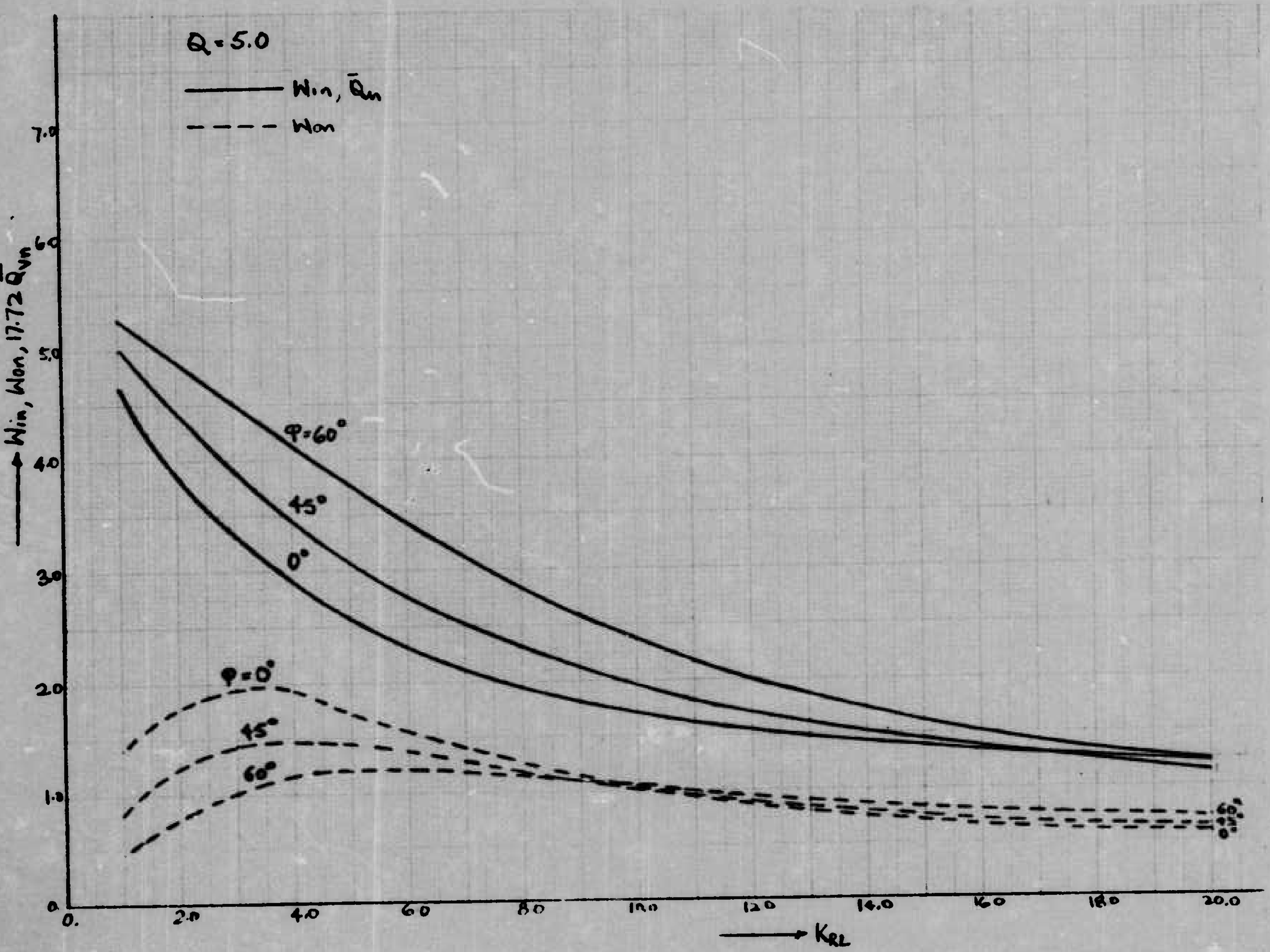

Figure 3.11c Normalized Values of Input Power, Output Power and Average Flow as a Function of K_{RL} for Different Values of $\emptyset$. Q = 5.0

Since input power is equal to the average flow through the valve times the constant supply pressure, P_S; the input power curves, when properly scaled ($\overline{Q}_{Vn}=W_{in}/17.72$) also represent $\overline{Q}_{Vn}$ the normalized average flow through the valve. The input power decreases monotonically as K_{RL} increases and is generally higher for larger ϕ. The output power peaks at K_{RL} approximately equal to 3.0 or 4.0 and then gradually decreases for higher values of K_{RL}. The maximum output power for a given Q is largest for $\phi = 0°$ and decreases as ϕ increases.

Figures 3.12 a, b, and c are mostly the replots of previous curves to assess the impact of increasing Q for a given value of ϕ on the various output parameters like η, α, and HDI. Figure 3.12a indicates that the value of ϕ has little effect on α up to K_{RL} equal to 6.0 for Q equal to 1 up to 10.0 whereas there is slight variation for higher values of K_{RL}. The maximum divergence (on the order of 15%) occurs at the highest value of K_{RL} shown. The efficiency also shows almost no variation up to K_{RL} equal to 5.0 whereas beyond that, the curves diverge rapidly and at K_{RL} equal to 20.0, n varies from .455 for Q equal to 5.0 to 0.72 for Q equal to 1.0. As expected the most significant variation in HDI occurs as Q is increased. For all values of Q the HDI curves dip down slightly as K_{RL} increases from 1.0 to about 4.0 and then rise for increasing K_{RL}. Thus it would seem that optimum value of K_{RL} for reducing harmonic distortion for a given Q is about 4.0.

Figures 3.13 a, b, and c are the plots of HDI for the flow through the valve (as compared to previous plots of HDI for flow through the load, i.e., flow after filtering) for Q equal to 1.0, 3.0, and 5.0 with varying ϕ. These curves are drawn to examine

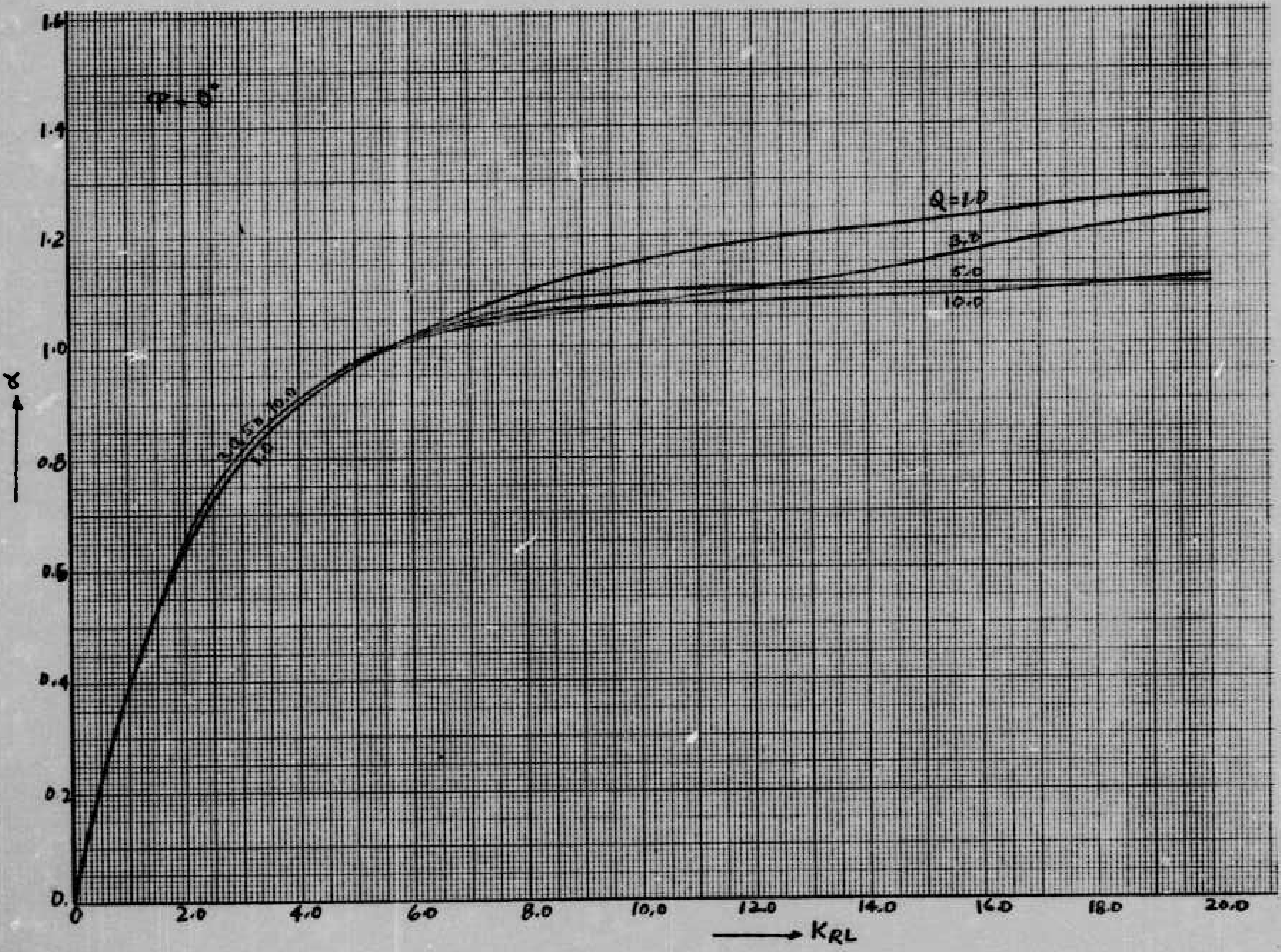

Figure 3.12a Variation of α as a Function of K_{RL} for Different Values of Q.
$\emptyset = 0°$

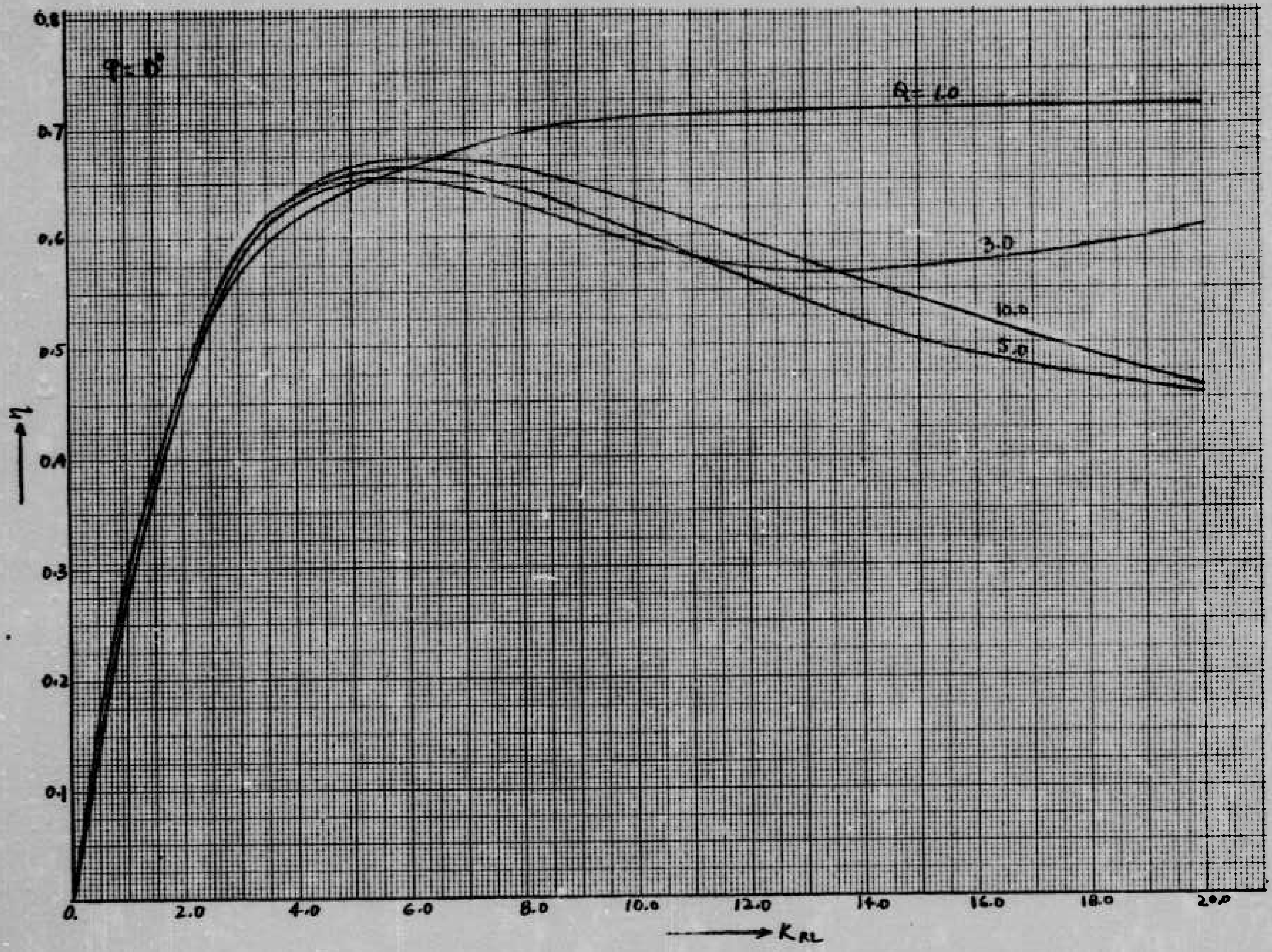

Figure 3.12b Variation of η as a Function of K_{RL} for Different Values of Q.
$\phi = 0°$

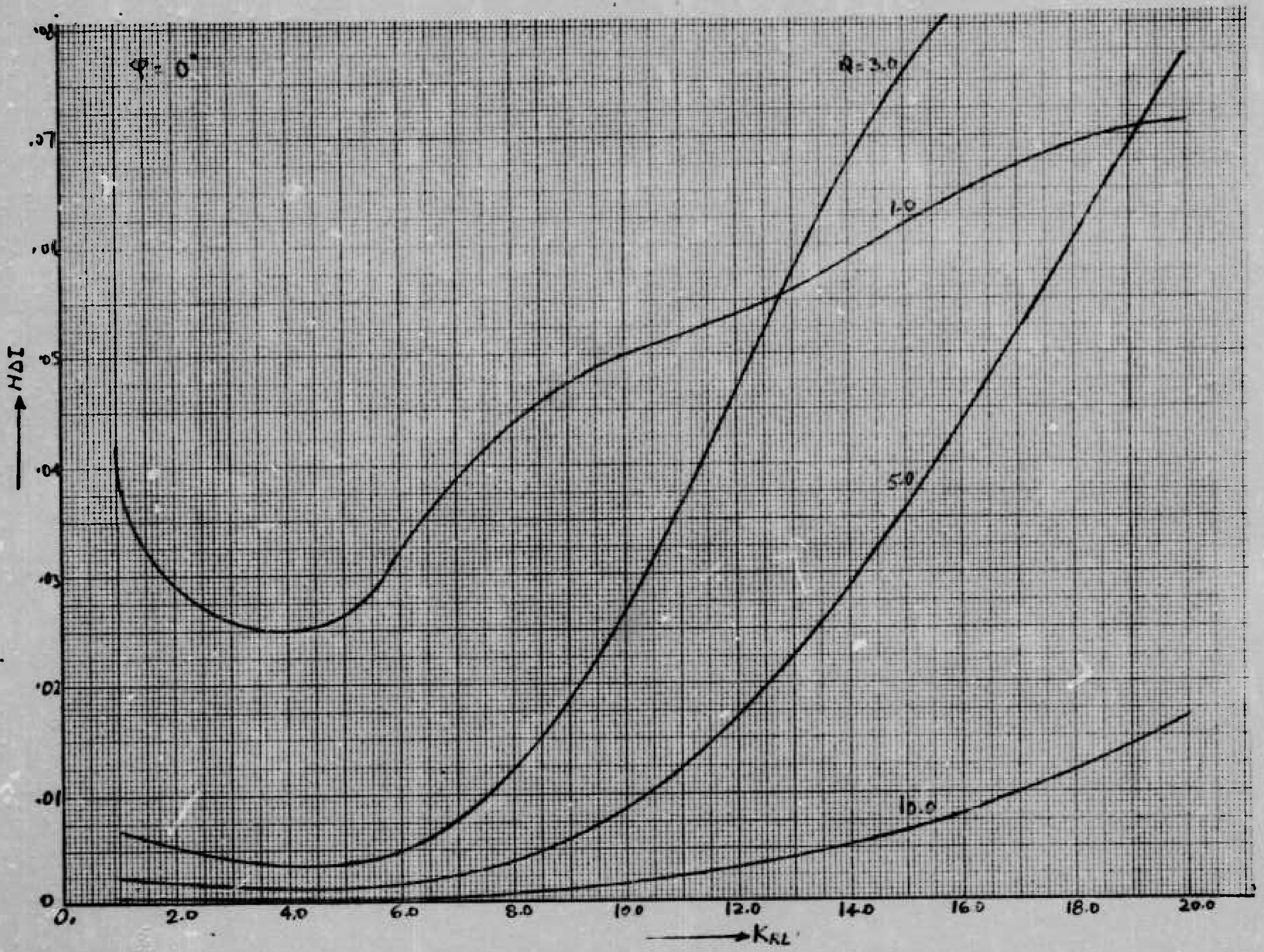

Figure 3.12c Variation of HDI as a Function of K_{RL} for Different Values of Q. $\phi = 0°$.

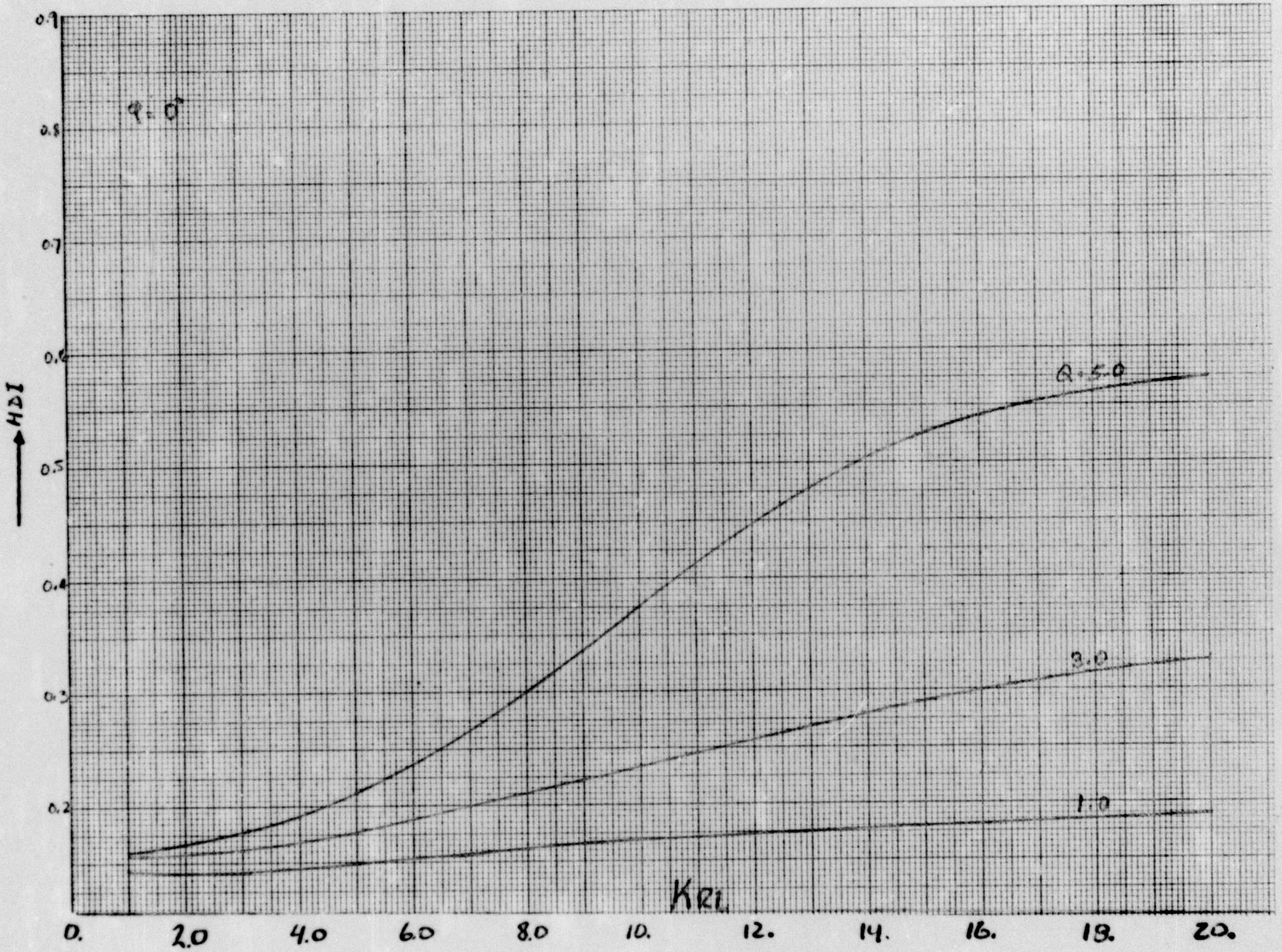

Figure 3.13a Variation of HDI of the Flow through the Valve as a Function of K_{RL} for Different Values of Q. $\phi = 0°$.

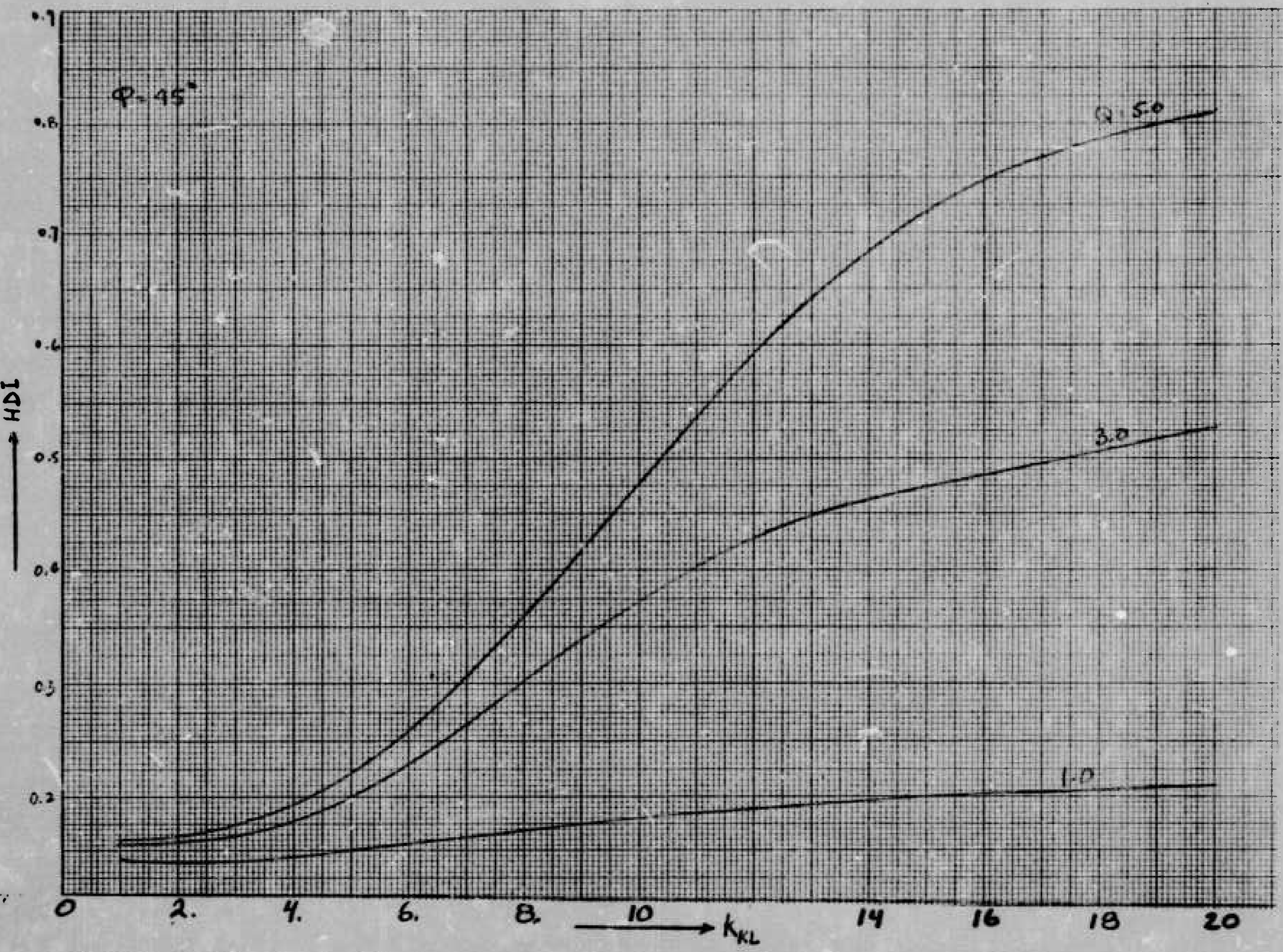

Figure 3.13b Variation of HDI of the Flow through the Valve as a Function of K_{RL} for Different Values of Q. Ø = 45°

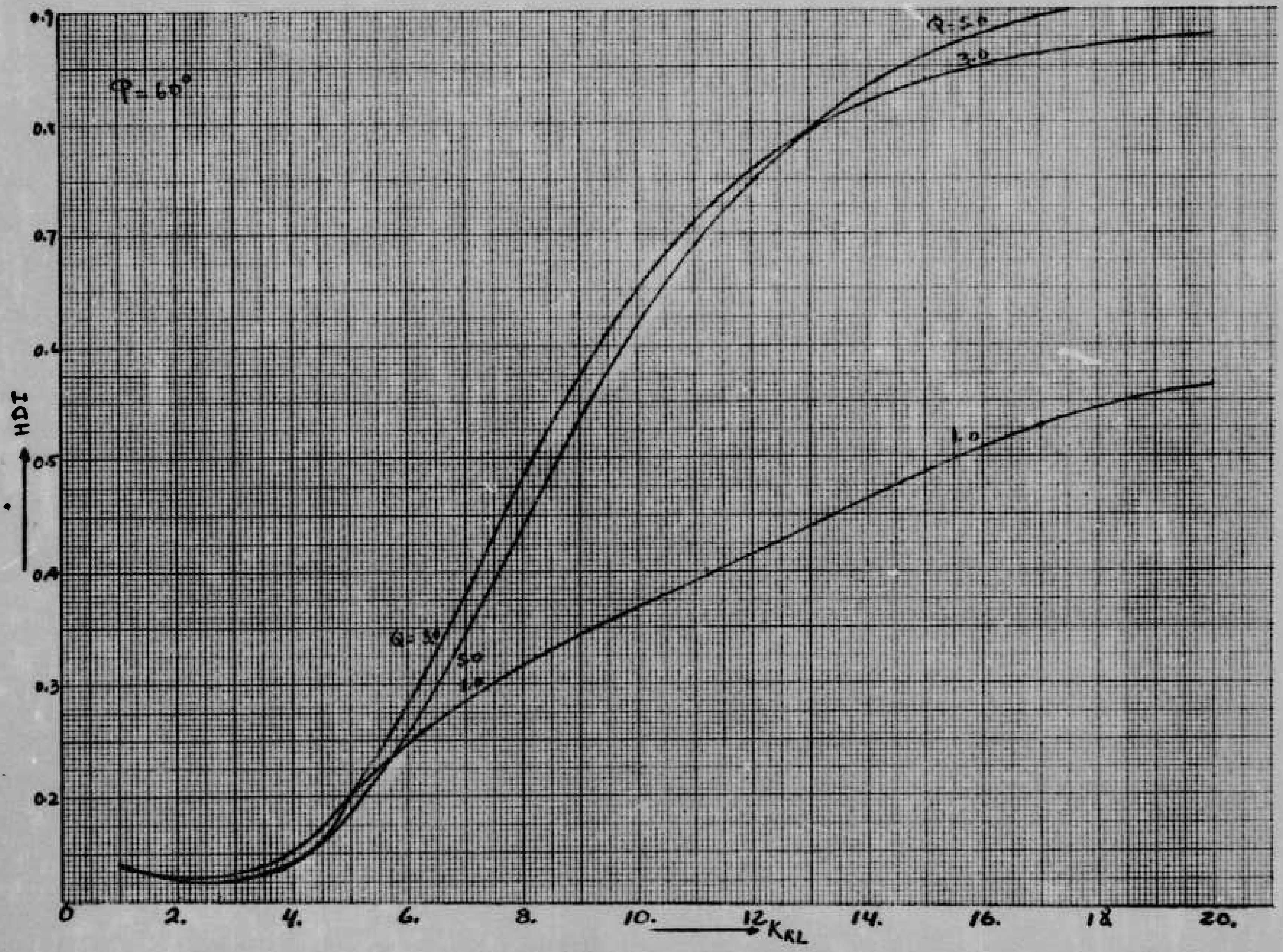

Figure 3.13c Variation of HDI of the Flow through the Valve as a Function of K_{RL} for Different Values of Q. Ø = 60°

the harmonic distortion before filtering and to measure the effectiveness of the designed filter.

Figures 3.14 a, b, and c are the plots of HDI as a function of K_{RL} for the double-ended device. These values are computed from the data of single orifice device as explained before. The harmonic distortion in general is correspondingly less than that for the single orifice device; the amount of reduction depends upon other parameters like Q, ϕ, and K_{RL}.

3.3.5 Trade-Off Considerations

The design objectives of a hydroacoustic transducer-amplifier are to achieve high efficiency, high output power and low harmonic distortion. Fortunately, much trade-off is not required as optimum conditions exist for a certain set of parameters. After a review of the description of the curves in the previous section, the following points are worth noting:

1) The optimum value of K_{RL} lies between 3.0 and 5.0 with slight variation depending on other parameters. In this range, the efficiency is highest or close to it, the harmonic distortion is minimum and the output power is at its peak. The device should be operated at its resonant frequency. The value of Q does not make significant effect on α or η in this range but affects HDI considerably. A higher value of Q would

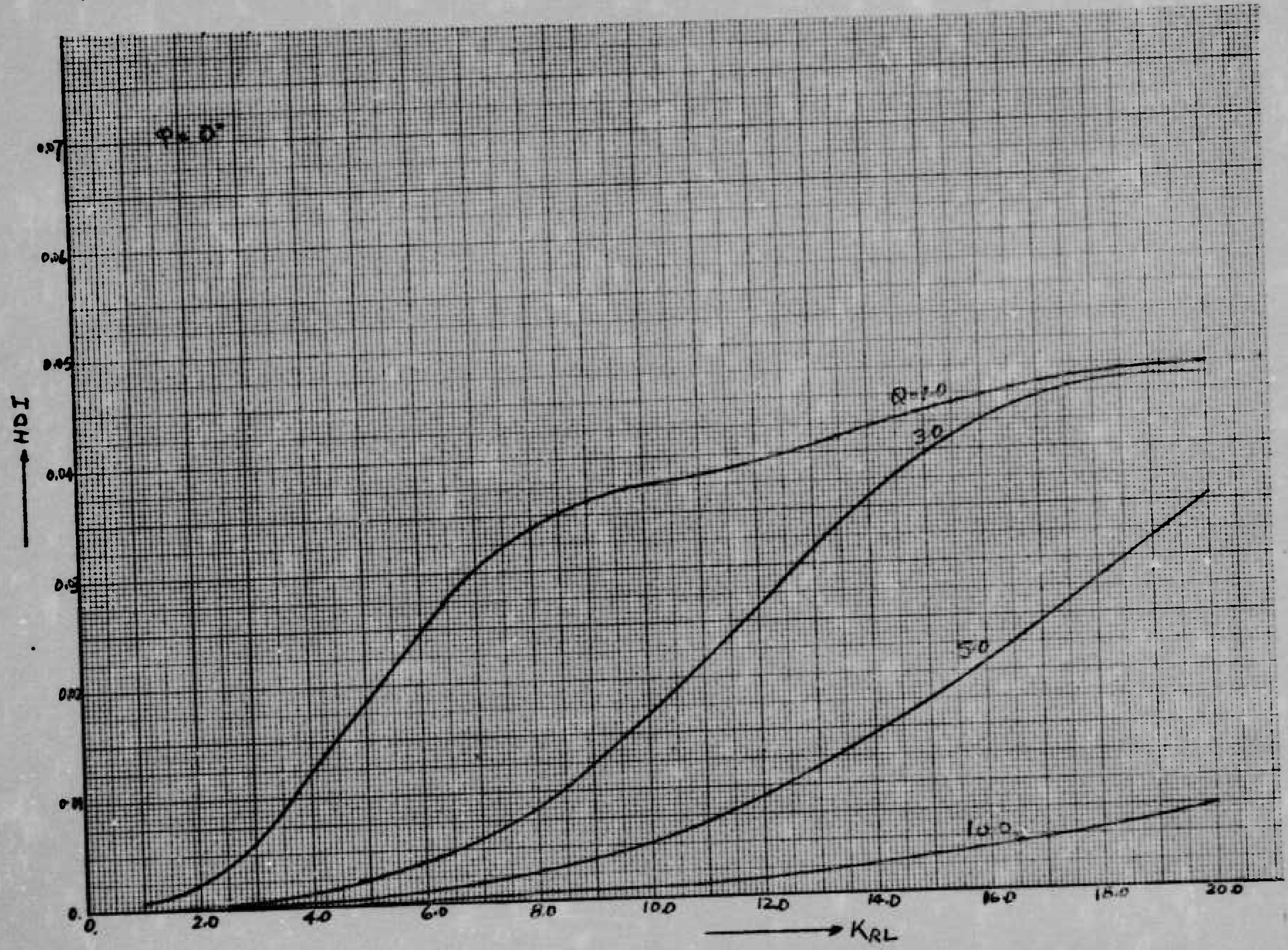

Figure 3.14a Variation of HDI for the Double-ended Device as a Function of K_{RL} for Different Values of Q. $\emptyset = 0°$

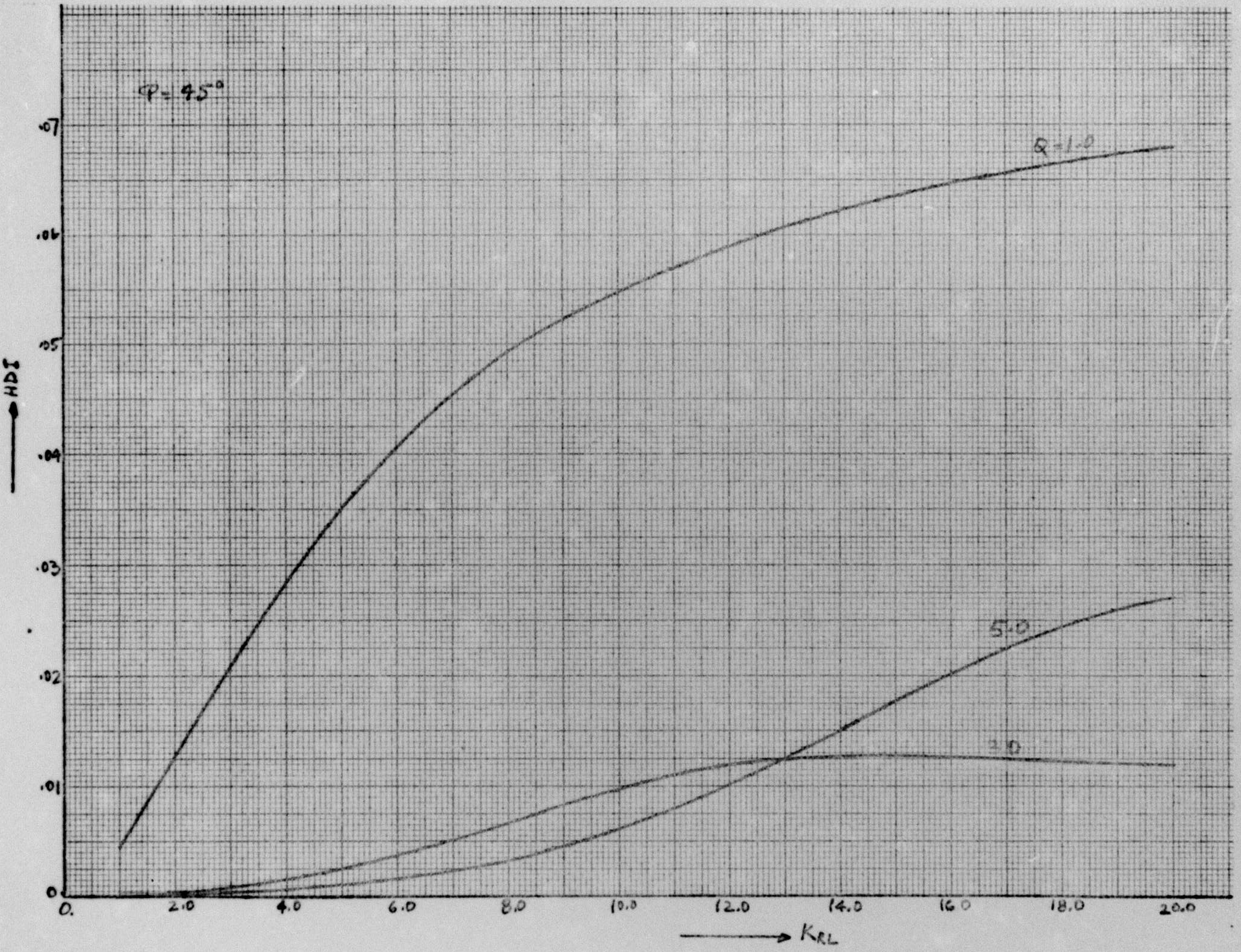

Figure 3.14b Variation of HDI for the Double-ended Device as a Function of K_{RL} for Different Values of Q. Ø = 45°

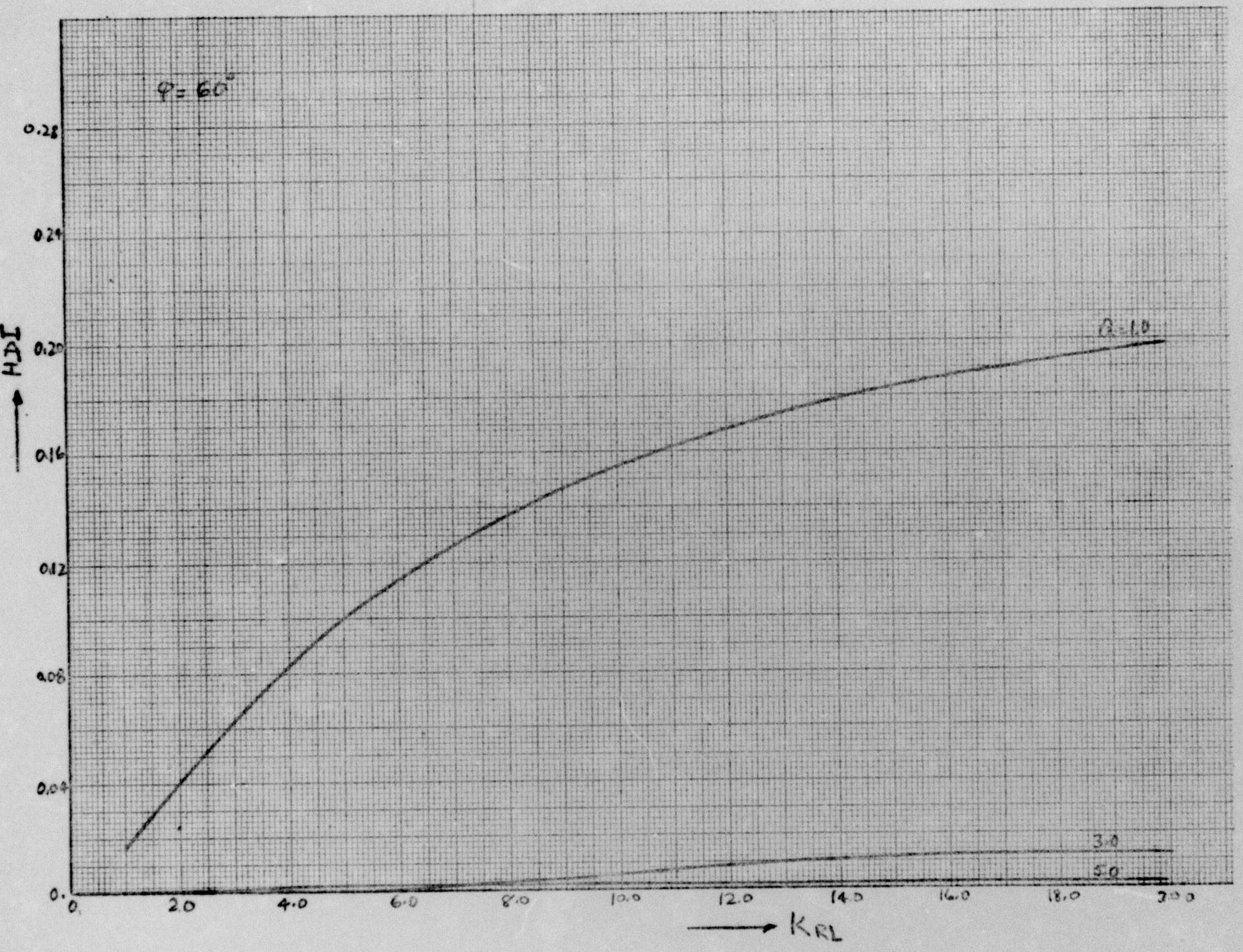

Figure 3.14c Variation of HDI for the Double-ended Device as a Function of K_{RL} for Different Values of Q. $\emptyset = 60°$

be desirable and an optimum value will be dictated by any physical constraints (size of cavities, etc.) and the permissible harmonic distortion. As seen in Figure 3.12c, the HDI is reduced dramatically when Q varies from 1.0 to 3.0 and only slightly when Q is raised from 3.0 to 5.0. The reduction is still smaller as Q varies from 5.0 to 10.0. Thus, if the device is to operate at a constant or almost constant driving frequency, an optimum or near optimum design can be easily achieved.

2) One trade-off would be an apparent choice between the single and double-ended device. The double-ended device leads to a low value of HDI; comparison of HDI curves in Figure 3.12c (single-ended) and in Figure 3.14a (double-ended) indicates roughly 50% reduction in the value of HDI. At K_{RL} about 4.0 and ϕ equal to 0° this reduction in an already small index is not very significant. However, at other values of ϕ and K_{RL}, the reduced index may require attention as a design factor. It should also be noted that for a given power rating, the double-ended device requires a larger stroke (by a factor of $\sqrt{2}$) and two metering edges.

3) If the driving frequency f varies over a certain range, the phase angle ϕ of the load will not be zero and will vary according to the value of f and Q. If Q is large, a given change in frequency will cause a greater change in phase angle relative to the change if Q was small for example:

$$Q = 1,\ \phi = 60°,\ w/w_o = .4569$$

$$Q = 5,\ \phi = 60°,\ w/w_o = .8417$$

As noted before, a higher value of ϕ will lead to greater harmonic distortion in general. Thus, depending upon the value of f a desirable value of Q should be selected from the curves. Such a value should be corresponding to high η and α a small value of HDI over the range of frequency change.

3.3.6 Other Areas of Investigation

Exploratory investigation was made in other fields related to acoustic flows as originally proposed while stress was placed on the areas which were of direct and immediate benefit.

High amplitude acoustic flows in pipes and through orifices are known to be turbulent although a criterion for determining the existence of turbulence (like critical Reynolds number for steady flows through pipes) is not available for acoustic flows. In the absence of a detailed mathematical analysis, the Reynolds number for such flows may be defined by $R_e = \frac{Ud}{\nu}$ where U is the average root mean square velocity. $U = \frac{2}{R^2}\int^R \overline{u}(y)y\,dy$, where

$$\overline{u}^2(r) = \frac{1}{T}\int_0^T \left(u\ (r,t)\right)^2 dt$$

R is the radius of the pipe, d is the diameter, u (r,t) defines the velocity field in the pipe, r represents the radial axis, T is the averaging time period, (much longer than the life time of large eddies), and ν is the kinematic viscosity.

For plane waves of the type

$$u = \hat{u} \exp (-\alpha_i X \exp (i [\alpha_r X-ct])$$

Where α_i is the attenuation factor, α_r is the wave number, $\hat{u}$ is the amplitude of the plane wave at X equal to zero, and c is the phase velocity.

A simpler way to define Reynolds number for acoustic flows is $Re = \frac{\hat{u}d}{\nu}$

Neglecting the contribution by heat conduction Kirchoff's formula for damping factor

$$\alpha_i = \frac{\omega}{dc}\sqrt{\frac{2\mu}{w\varepsilon}}$$

μ is the coefficient of viscosity. Since turbulence increases the dissipation losses, its effect can be accounted for by replacing the coefficient of viscosity μ by the eddy viscosity coefficient ε. Lacking the mathematical tools to handle the theory to turbulence, the use of eddy viscosity has been a familiar way to estimate the additional losses. However, there is no way to estimate analytically. The value of ε is generally determined from experimental data regarding steady flow in pipes etc. Binder (*) used a similar technique for measuring the damping of large amplitude vibrations of a fluid in a pipe, and by adjusting the value of ε found a fair agreement with experiment. A more sophisticated

---

*Binder, R.C., "The Damping of Large Amplitude Vibrations of a Fluid in a Pipe", Journal of the Acoustic Society of America; P41, Volume 15, 1943.

handle on the turbulence losses will require an intensive look into experiments on purely acoustic and mixed (steady and acoustic) flows where loss measurements have been made. An approximate analytical model is also probably feasible on lines of the turbulent flow through jets and pipes where eddy viscosity is related to other parameters like velocity. In the mean time, a crude determination may be made by the approach defined above.

DISTRIBUTION:

Commanding Officer Naval Coastal Systems Laboratory Panama City, Florida 32401 Attn: Rufus Cook, Code 722	N61331	1
Commander Naval Ship Systems Command Department of the Navy Washington, D.C. 20360 Attn: Code PMS 302-42	N00024	3
Commander Naval Ship Systems Command Department of the Navy Washington, D.C. 20360 Attn: Code 2052	N00024	4
Director Naval Research Laboratory Washington, D.C. 20390 Attn: Sam Hanish, Code 8150	N00173	1
Director Naval Research Laboratory Underwater Sound Reference Division P.O. Box 8337 Orlando, Florida 32806 Attn: Ivor Groves	N62190	1
Commander Naval Ship Research and Development Center Annapolis, Maryland 20402 Attn: Dr. A. Lebovits	N61533	1
Defense Documentation Center Cameron Station (Bldg. 5) 5010 Duke Street Alexandria, Virginia 22314	S47031	12
Naval Ship Engineering Center Center Building Prince George Center Hyattsville, Maryland 20782 Attn: 60241	N65197	1

DISTRIBUTION(Continued:

Defense Contract Administrative Service Division Rochester District 100 State Street Rochester, New York 14614	None	1
Aerojet Electro Systems Company 1100 W. Hollyvale Street Azursa, California 91702 Contract N00024-72-C-1200	91137	1
Commander Naval Undersea Research & Development Center San Diego, California 92132 Attn: John Hickman, Code 601	N66001	1
Commanding Officer Naval Underwater Systems Center New London Laboratory New London, Conn. 06320 Attn: Ed Parssinen, Code 2220	N70024	5